

See discussions, stats, and author profiles for this publication at: <https://www.researchgate.net/publication/268514496>

# Hydrogen Storage with Spectroscopic Identification of Chemisorption Sites in Cu-TDPAT via Spillover from a Pt/Activated Carbon Catalyst

ARTICLE in THE JOURNAL OF PHYSICAL CHEMISTRY C · NOVEMBER 2014

Impact Factor: 4.77 · DOI: 10.1021/jp507395p

---

CITATION

1

READS

45

## 9 AUTHORS, INCLUDING:



Cheng-Yu Wang

Feng Chia University

12 PUBLICATIONS 265 CITATIONS

[SEE PROFILE](#)



Qihan Gong

PetroChina Company Limited

20 PUBLICATIONS 980 CITATIONS

[SEE PROFILE](#)



Jing Li

Case Western Reserve University

173 PUBLICATIONS 2,819 CITATIONS

[SEE PROFILE](#)



Angela D Lueking

Pennsylvania State University

45 PUBLICATIONS 774 CITATIONS

[SEE PROFILE](#)

# Hydrogen Storage with Spectroscopic Identification of Chemisorption Sites in Cu-TDPAT via Spillover from a Pt/Activated Carbon Catalyst

Cheng-Yu Wang,<sup>†</sup> Jennifer L. Gray,<sup>‡</sup> Qihan Gong,<sup>§</sup> Yonggang Zhao,<sup>§</sup> Jing Li,<sup>§</sup> Emmanuel Klontzas,<sup>||</sup> George Psolfogiannakis,<sup>||,⊥</sup> George Froudakis,<sup>||</sup> and Angela D. Lueking<sup>\*,†,‡,§,||,#</sup>

<sup>†</sup>Department of Energy and Mineral Engineering, Pennsylvania State University, University Park, Pennsylvania 16802, United States

<sup>‡</sup>Materials Characterization Laboratory, Pennsylvania State University, University Park, Pennsylvania 16802, United States

<sup>§</sup>Department of Chemistry & Chemical Biology, Rutgers University, Piscataway, New Jersey 08854, United States

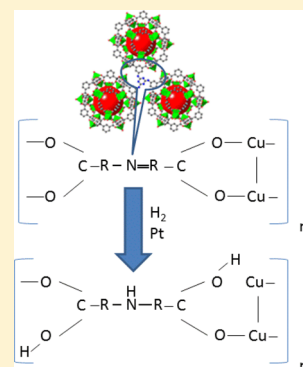
<sup>||</sup>Department of Chemistry, University of Crete, Voutes, Heraklion, Greece

<sup>⊥</sup>Department of Mechanical Engineering, Pennsylvania State University, University Park, Pennsylvania 16802, United States

<sup>\*</sup>Department of Chemical Engineering and EMS Energy Institute, Pennsylvania State University, University Park, Pennsylvania 16802, United States

## S Supporting Information

**ABSTRACT:** Hydrogen spillover to the Cu-TDPAT (TDPAT = 2,4,6-tris(3,5-dicarboxyphenylamino)-1,3,5-triazine) metal–organic framework is probed with adsorption measurements, *ex situ* characterization techniques, and density functional theory (DFT) calculations. At 1 bar and 300 K, hydrogen chemisorption to Pt/AC/Cu-TDPAT exceeds that expected for physisorption by 8-fold, which is attributable to both catalyst insertion and the creation of structural defects. Hydrogenation of (a) the Cu–O–C bond of the Cu paddlewheel, (b) the  $sp^2$  N heterocycle, and (c) the secondary amine is demonstrated with *ex situ* spectroscopy. Exothermic (with respect to  $H_2$ ) hydrogenation at the Cu–O–C bond of the paddlewheel is substantiated by DFT. However, hydrogenated Cu–O–C is metastable, as evidence for dissociation is found at higher temperature (i.e., 473 K  $H_2$ ). DFT calculations demonstrate hydrogenation of the N groups may occur exothermically only for a charged ligand, suggestive that defects may contribute to hydrogen chemisorption. At high pressure, slow adsorption rates and material instability render the material unsuitable for practical hydrogen storage applications.



## 1. INTRODUCTION

Hydrogen is a potential clean energy carrier with the highest chemical energy density per molecular mass. Metal–organic frameworks (MOFs)<sup>1–3</sup> have been proposed as a solid-state adsorbent to increase the overall gravimetric and volumetric density of  $H_2$ , as MOFs have high surface area (SA), adjustable pore size, and tunable chemical functionality.<sup>1</sup> Physisorption of  $H_2$  to MOFs requires cryogenic conditions to approach the U.S. Department of Energy (DOE) hydrogen storage targets (5.5 wt % by 2017 and ultimate goal 7.5 wt %),<sup>4</sup> which leads to a number of practical challenges in designing a mobile fuel cell vehicle. Hydrogen spillover has been proposed as a means to increase the  $H_2$  adsorption temperature to the more practical DOE target temperature window (−40 to 85 °C).<sup>5,6</sup> Hydrogen spillover involves incorporation of a catalyst to dissociate  $H_2$  into an active H species,<sup>7</sup> which then diffuses away from the catalyst and weakly chemisorbs to the nearby support.<sup>8</sup> Catalyzed MOFs reportedly adsorb up to 4 wt % (excess) hydrogen at 100 bar and 300 K.<sup>9–11</sup> In addition to MOFs,<sup>9–19</sup> hydrogen spillover also increases the operative adsorption temperature in carbons<sup>5,6,20–28</sup> and zeolites.<sup>29</sup> Inactive catalysts, however, decrease the hydrogen

uptake relative to that expected for physisorption under the same conditions.<sup>30–34</sup>

Mechanistic insight into hydrogen spillover has been sought for over 70 years,<sup>7,35</sup> with recent renewed interest in identifying the specific binding site for optimization of hydrogen storage. Inelastic neutron scattering (INS) provided evidence for formation of a new C–H bond<sup>36–38</sup> and/or loss of molecular hydrogen<sup>26</sup> via spillover to carbon-based supports. Diffuse reflectance infrared Fourier transform spectroscopy (DRIFTS) was used to demonstrate formation of weak covalent C–H/C–D bonds but was accompanied by irreversible water formation and surface deactivation.<sup>38</sup> In our laboratory, we utilized *in situ* Raman spectroscopy to demonstrate high mobility and reversibility of a weak C–H/C–D bond but with high cyclability and no evidence for water formation.<sup>39</sup> High room temperature mobility of H chemisorbed on carbon requires surface heterogeneities to render the process exothermic with reasonable diffusion barriers.<sup>40</sup> In MOFs, however, spectroscopic evidence

Received: July 23, 2014

Revised: October 10, 2014

Published: October 13, 2014

of the active spillover binding sites is more limited. Temperature-programmed desorption (TPD) demonstrated room temperature desorption of H<sub>2</sub> from IRMOF-8 catalyzed by a Pt/AC catalyst after carbonization of D-glucose,<sup>11</sup> but the specific binding sites were not identified. We used *ex situ* Fourier transform infrared (FTIR) spectroscopy to demonstrate conversion of the carboxyl groups of Cu-BTC (Cu<sub>3</sub>(BTC)<sub>2</sub>(H<sub>2</sub>O)<sub>3</sub>, BTC = benzene tricarboxylate) to carboxylic acid after room-temperature hydrogen exposure without degradation of the Cu-BTC structure.<sup>8</sup> At higher temperature (i.e., 150 °C), Yang et al.<sup>41</sup> found hydrogenation of Pt-doped Cu-BTC led to both Cu reduction and structural degradation, whereas Pt-doped MIL-53 and ZIF-8 did not show degradation under these conditions. In these studies, no evidence for Cu reduction was presented after room-temperature H<sub>2</sub> exposure.

MOFs remain a promising option for designing hydrogen spillover materials, as the ability to tailor specific chemical functional groups of the organic ligands would provide a means to optimize spillover receptor sites.<sup>18</sup> Density functional theory (DFT) calculations suggest the organic ligand may be fully hydrogenated, and the stoichiometric uptake is consistent with certain experimental measurements.<sup>11,42–44</sup> However, discrepancies between experimental measurements suggest the spillover mechanism is still not well understood, particularly for a chemically heterogeneous MOF surface. To further complicate experimental interpretation and modeling, structural degradation of MOFs plagues many of the reports, with substantial decreases in the MOF SA<sup>15,19,45–49</sup> and/or changes in the PXRD patterns.<sup>10</sup> This motivated us to explore how various catalytic doping methods affect the structural stability of MOFs,<sup>50</sup> and we found that a “pre-bridge” (PB) technique<sup>51,52</sup> led to retention of MOF SA and structure, even after hydrogen exposure at elevated temperatures. The PB technique introduces a highly dispersed prereduced Pt/AC catalyst prior to MOF crystal growth, and thus, the MOF precipitates around the catalyst. Doping of Cu-TDPAT ([Cu<sub>3</sub>(TDPAT)(H<sub>2</sub>O)<sub>3</sub>] (abbreviated as T; TDPAT = 2,4,6-tris(3,5-dicarboxylphenylamino)-1,3,5-triazine; see Figure 1) via the PB technique led to the highest hydrogen uptake at 300 K and 1 bar relative to any previous reports of catalyst-doped MOFs under these conditions. Here, we probe the nature of the H binding sites to T using *ex situ* characterization (utilizing PXRD, FTIR, and X-ray photoelectron spectroscopy (XPS)), hydrogen adsorption measurements, and DFT calculations. We compare the interaction of H<sub>2</sub> with T and PB-T to ascertain the effect of catalyst, including the effect of temperature and H<sub>2</sub> pressure on structural changes, and the accessibility of hydrogen to the T ligand. We propose a metastable, defected structure that leads to enhanced hydrogen adsorption via spillover. The complex chemical topology of the TDPAT ligand (which includes (a) sp<sup>2</sup> hybridized carbons, (b) sp<sup>2</sup> N heterocycles on the center ring, and (c) amine-type NH groups in the branch, as labeled in Figure 1) provides a unique means to probe activity of these functional groups to bind spilled over hydrogen.

## 2. EXPERIMENTAL SECTION

### 2.1. Sample Preparation. 2.1.1. Synthesis of Cu-TDPAT.

Cu-TDPAT (T) was synthesized via solvothermal procedures,<sup>53</sup> in which 0.68 mmol of Cu(NO<sub>3</sub>)<sub>2</sub>·6H<sub>2</sub>O and 0.05 mmol of H<sub>6</sub>TDPAT were dissolved in 2 mL of DMA (dimethylacetamide) solvent with 2 mL of DMSO (dimethyl sulfoxide), 0.2 mL of H<sub>2</sub>O, and 0.9 mL of HBF<sub>4</sub>. The mixture was kept in a capped glass vial at 358 K for 3 days and cooled down in a programmable

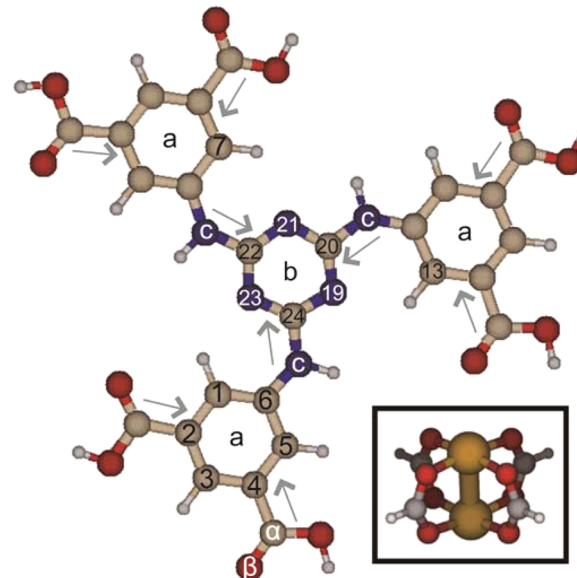


**Figure 1.** H<sub>6</sub>TDPAT (TDPAT = 2,4,6-tris(3,5-dicarboxylphenylamino)-1,3,5-triazine) ligand, which contains (a) external sp<sup>2</sup>-hybridized outer carbon rings, (b) sp<sup>2</sup>-hybridized N heterocycles in a center ring, and (c) three branches with secondary-amine sites. The labels correspond to the hydrogenation order in Tables 1 and 2, and the gray arrows refer to directional diffusion as discussed in the text. Inset: The Cu paddlewheel (Cu PDW). In the T structure, the TDPAT ligand replaces the formate in the image shown. Atom colors are as follows: C = gray, O = red, N = blue, H = white, Cu = brown.

oven with a 0.1 °C/min speed. Blue polyhedron crystals ([Cu<sub>3</sub>(TDPAT)(H<sub>2</sub>O)<sub>3</sub>]·10H<sub>2</sub>O·5DMA) were collected and washed with 10 mL of DMA three times and then immersed in methanol for solvent exchange. Subsequent discussion will refer to the various surface sites in the TDPAT ligand with subscripts referring to the positions labeled in Figure 1.

T was characterized after exposure to hydrogen in different environments, including: (a) 300 K at 1 bar (T-300-1), (b) 300 K at 70 bar (T-300-70), and (c) 423 K in 1 bar H<sub>2</sub> (T-423-1). The 300 K measurements consisted of extended exposure over the course of multiple adsorption isotherms, whereas the 423 K exposure was for 1 h in a tube furnace with flowing hydrogen. The above nomenclature, i.e., sample name-temperature (in K)-pressure (in bar), was used for other samples discussed in this paper.

**2.1.2. Direct Doping (DD) of Pt Catalyst.** T was direct-doped (DD) with Pt by adopting techniques from Sabo et al.<sup>48</sup> to produce DD-T-423-1, as reported previously.<sup>50</sup> T powder was placed on a watch glass with a magnetic stirrer, and platinum acetylacetonate (Pt(acac)<sub>2</sub>) (Aldrich) dissolved in 2 mL of DEF (diethylformamide) (TCI) was added to the MOF substrate to produce an expected 5 wt % Pt. The slurry was stirred and dried in Ar flow for 2 h and in a vacuum (<10<sup>-2</sup> mbar) at room temperature overnight. The mixture was preheated at 353 K for 2 h in Ar flow, and then raised to 423 K for 1 h in H<sub>2</sub> flow. As the synthesis of DD-T-423-1 includes a 423 K reduction, the sole effect of H<sub>2</sub> at 300 K could not be explored.

**2.1.3. Synthesis of Catalyst-MOF Composite via the Pre-Bridge (PB) Technique.** A “pre-bridge” (PB) doping technique dispersed 5 wt % Pt/AC into the T synthesis solution to yield a 1:19 weight ratio of Pt/AC to T, labeled as PB-T, with a final Pt content of 0.25 wt %. Detailed procedures can be found in our previous paper.<sup>50</sup> In brief, the Pt/AC catalyst utilized the

ultrasound-assisted wet impregnation of chloroplatinic acid ( $\text{H}_3\text{PtCl}_6$ ) method<sup>17,23</sup> to dope 5 wt % Pt on Maxsorb activated carbon (AC, CO., LTD, Japan; provided by the National Renewable Energy Laboratory, CO). The resulting Pt/AC catalyst consisted of well dispersed 1–2 nm Pt nanoparticles with a  $\text{N}_2$  BET surface area of ~2900  $\text{m}^2/\text{g}$  (about 90% compared to AC). The PB-T sample was synthesized by ultrasonication and stirring the reaction mixture (0.68 mmol of  $\text{Cu}(\text{NO}_3)_2 \cdot 6\text{H}_2\text{O}$ , 0.05 mmol of  $\text{H}_6\text{TDPAT}$ , 1.8 mg of Pt/AC dispersed in 2 mL of DMA, 2 mL of DMSO, 0.2 mL of  $\text{H}_2\text{O}$ , and 0.9 mL of  $\text{HBF}_4^-$ ) overnight. The sample was then kept in either a capped glass vial or a Teflon-lined autoclave and reacted at 383 K for 3 days. DMA was used to wash the product, and solvent exchange by methanol was carried out every hour for a week. AC-T was prepared with the same procedures but with omission of Pt, i.e., dispersing undoped AC in the reaction mixture. PB-T was exposed to the same hydrogen environments described above, i.e., hydrogen at 300 K and 1 bar (PB-T-300-1), 300 K and 70 bar (PB-T-300-70), and 423 K and 1 bar (PB-T-423-1). In addition, PB-T-300-70 and PB-T-423-1 were subsequently heated in 1 bar argon at 400 K (a “D” for desorption was appended to the sample name as PB-T-300-70-D and PB-T-423-1-D). The desorption treatments were limited to XPS characterization, as the heating was done on the XPS stage in a tube furnace.

**2.2. Characterization.** The powder X-ray diffraction (PXRD) patterns were observed from a PANalytical XPert Pro MPD theta–theta diffractometer, operated at 45 kV, 40 mA, with minimum  $2\theta = 5^\circ$ , step size  $0.026^\circ$ , scan speed  $0.067^\circ/\text{s}$ , and Cu  $\text{K}\alpha$  ( $\lambda = 1.543 \text{ \AA}$ ) X-ray source. For plotting, the PXRD patterns were normalized by the peak with the highest intensity. Fitting of the PXRD patterns to provide the full-width half-maximum (fwhm) are provided in the Supporting Information. X-ray photoelectron spectroscopy (XPS) used a Kratos Axis Ultra with a monochromatic Al  $\text{K}\alpha$  X-ray source operated at 14 kV and 20 mA in hybrid slot mode. The samples were placed on carbon tape to fixate the material to either copper or silicon wafers. The survey scans were done using a pass energy of 80 eV, with a 0.5 eV step size and 150 ms dwell time. In the high-resolution scan, we used a pass energy of 20 eV and a step size of 0.1 eV. The dwell time was chosen on the basis of the relative height of the peak in the survey scans and therefore would vary for the different peaks. Surface residual charges in high-resolution spectra were corrected on the basis of C 1s assigned to 284.5 eV. The curve fitting and peak assignment were based on the *Handbook of X-ray Photoelectron Spectroscopy*,<sup>54</sup> assignments of N groups in T were based on melamine.<sup>55</sup>

The FTIR was measured in a Bruker IFS 66/S Spectrometer with attenuated total reflectance (ATR), as the large T particle size led to full absorbance in transmittance mode. Water exposure was unavoidable during atmospheric ATR experiments, and the hydrophilic T tended to adsorb water, as was evident by both a color change (from blue to green) and a broad OH stretch from 2700 to 3700  $\text{cm}^{-1}$  (see Figure S1A, Supporting Information). A broad OH stretch mode from water adsorption made definitive assignment of FTIR modes in this region difficult, including those associated with amine groups; thus, this data was included in the Supporting Information only. Sequential FTIR measurements showed no changes in the “fingerprint” region over the time scale of the measurements, suggesting water adsorption had no effect on the modes in the fingerprint region discussed below. The FTIR spectrum of the  $\text{H}_6\text{TDPAT}$  ligand and the as-received Cu-TDPAT were collected in the presence of methanol solvent, and thus exhibit a C–O stretch at 1001

$\text{cm}^{-1}$ ,<sup>56,57</sup> not found in the other samples. Assignment of the basic FTIR features was as follows: The acid  $\text{H}_6\text{TDPAT}$  ligand has a C–O stretch at 1250–1300  $\text{cm}^{-1}$  and a C=O stretch at 1680–1690  $\text{cm}^{-1}$ , consistent with the presence of an aromatic carboxylic acid.<sup>57,58</sup> Upon incorporating the TDPAT ligand into the T crystal structure, the C–O bonds become symmetric, and these features are lost. The TDPAT ligand also has a C–H bend at 750–800 and 860–900  $\text{cm}^{-1}$ ,<sup>58</sup> C–N stretch at 1050–1360  $\text{cm}^{-1}$ ,<sup>55,59</sup> aromatic C=C stretch at 1450–1600  $\text{cm}^{-1}$ ,<sup>8,58,60</sup> and C=N stretch at 1615–1700  $\text{cm}^{-1}$ .<sup>55,61</sup> Features associated with the Cu paddlewheel (PDW) are found at 492 and 774  $\text{cm}^{-1}$ , and assigned to a Cu–O stretch and bend vibration, respectively, for reasons discussed in section 3.2.1 below. These Cu PDW features are of course absent in the  $\text{H}_6\text{TDPAT}$  ligand and pronounced in the as-received T. Select samples were performed in parallel on FTIR in transmittance mode with KBr pellet to verify no significant peak shifts occurred in ATR mode (data not shown).

High-pressure  $\text{H}_2$  adsorption measurements at 70 bar were obtained by a differential volumetric analyzer. Single point measurements were conducted, as this leads to the greatest measurement sensitivity,<sup>62</sup> and allows us to collect the full adsorption kinetics from a vacuum. The double-sided unit enables simultaneous adsorption measurements to a blank reference cell in hydrogen to minimize the effects of volume calibration, gas nonidealities, and temperature variations.<sup>62</sup> Our unit does not have external temperature control, as differential units tend to be fairly insensitive to small temperature fluctuations (see calculations<sup>62</sup>); however, to compensate for observed 24 h cyclic temperature variations, all experiments were started at the same time of day. The He blanks provide an indication of the effect of the cyclic temperature variations on the adsorption signal, and were performed sequentially after  $\text{H}_2$  measurements to confirm slow adsorption rates were not due to gas leakage. Prior to the  $\text{H}_2$  adsorption measurement, PB-T samples were pretreated at 393 K for 10 h under a high vacuum ( $10^{-6} \text{ mbar}$ ) on an ancillary degas station. Sequential He measurements were performed after an intermediate vacuum pretreatment of 12 h but without disconnecting the sample from the adsorption unit. In certain cases, sequential  $\text{H}_2$  measurements were performed on the same sample batch, repeating the high-vacuum pretreatment on the ancillary degassing station. In discussion of the high-pressure adsorption results below, the sample nomenclature refers to batch number followed by sequential ( $\text{H}_2$ ) measurement number.

**2.3. Density Functional Theory (DFT).** Quantum chemistry calculations were performed within the framework of DFT applying the resolution of identity (RI) approximation<sup>63</sup> in our calculations. The B-P86 exchange-correlation functional<sup>64,65</sup> along with the def2-TZVP basis set<sup>66</sup> (with the corresponding auxiliary basis set for the RI approximation) was used. The BP86 GGA functional generally shows excellent performance in predicting vibrational frequencies and good performance in energetics,<sup>67</sup> although the ability of a given functional to predict energy quantities for transition metals is very reaction-specific.<sup>68</sup> The def2-TZVP basis set is a very reliable accurate basis set,<sup>66</sup> providing a reasonable compromise between accuracy and computational time, given the larger uncertainties associated with the choice of functional and model size. All structures were optimized without any symmetry constraints, and the optimized minimum-energy structures were verified as stationary points on the potential energy surface by performing analytical harmonic vibrational frequency calculations. Different spin states were evaluated for each model in order to find the spin state that

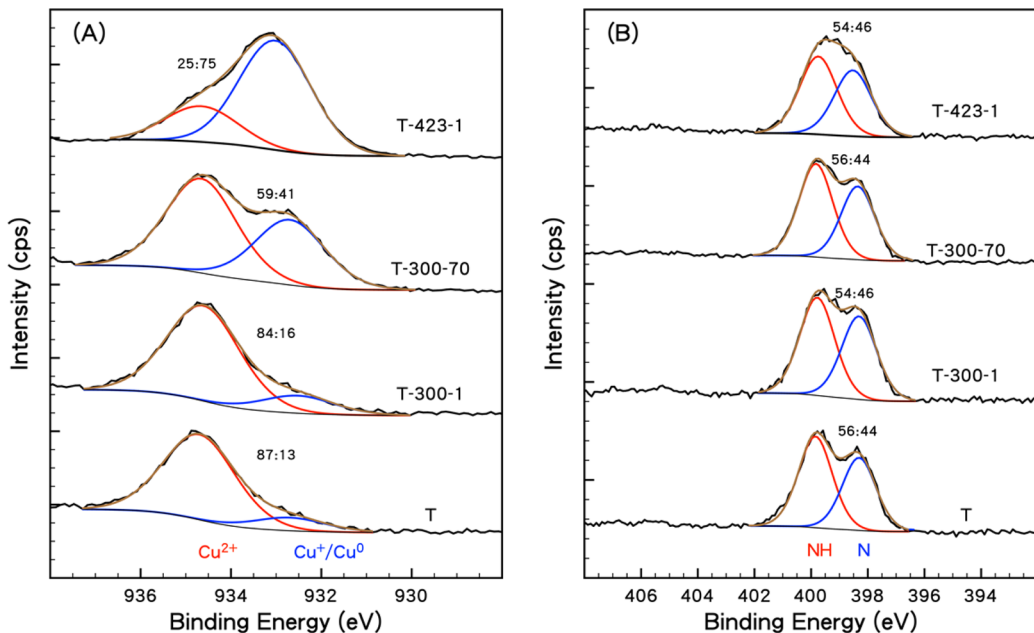


**Figure 2.** XPS spectra of pure T, including (A) Cu 2p 3/2 and (B) N 1s, after various H<sub>2</sub> exposures. Numbers following the sample name indicate the temperature (in K) and pressure (in bar) of H<sub>2</sub> exposure. The subpeak ratio is listed. An increase in the Cu<sup>+</sup>/Cu<sup>0</sup> peak is observed after all exposures to H<sub>2</sub>, but no appreciable variation in nitrogen is observed.

corresponds to the ground state. Additional calculations (not shown) replaced the formate ligands with four benzene carboxylate ligands, and calculated energies were relatively invariant for these two organic ligands, suggesting the ligand choice did not affect the Cu PDW calculations. Potential hydrogenation sites on the Cu PDW were explored by placing 1, 2, 4, 6, or 8 H atoms at various locations on the Cu PDW and allowing for structural relaxation. Structures that were both stable and exothermic with respect to molecular H<sub>2</sub> are reported. DFT predicted frequencies were calculated analytically, and multiplied by the recommended correction factor (0.96<sup>69</sup>) for the functional. Peak assignments were attributed to specific bonds using TMoleX for visualization, and also comparing the predicted frequencies to experimental data for similar structure (see Figure S2, Supporting Information). Hydrogenation energies and frequencies for a truncated Cu PDW, i.e., Cu atom pair with four formate ligands (see inset in Figure 1), were calculated with the def2-TZVP basis set.<sup>66</sup> To consider hydrogenation of the ligand, H<sub>6</sub>TDPAT was used as a molecular model using the SVP basis set.<sup>66</sup> In general, all possible remaining unique hydrogenation sites were considered; the exceptions were in sites 8–12 and 14–18, where, due to symmetry, it was assumed the order would follow 1–6. Calculations were performed both with the oxygen atoms of the carboxylate held in place and for the fully relaxed structure. All DFT calculations were performed with the TURBOMOLE<sup>70</sup> program.

### 3. RESULTS AND DISCUSSION

**3.1. Spectroscopic Evidence of Cu-TDPAT Hydrogenation.** *3.1.1. Baseline Data for Undoped Cu-TDPAT and PB-T.* The Cu-TDPAT sample (T) served as a control for subsequent tests for the catalyst-doped samples. Prior to H<sub>2</sub> exposure, XPS spectra of T consisted of a major (87%) Cu<sup>2+</sup> peak at 934.5 eV, associated with Cu<sup>2+</sup> in the PDW, and a small (13%) reduced Cu<sup>+</sup>/Cu<sup>0</sup> peak at 932.4 eV (Figure 2A). In the absence of any reduced Cu phase in PXRD (Figure 3), the Cu<sup>+</sup>/Cu<sup>0</sup> peak was attributed to structural defects.<sup>71</sup> The N 1s spectra (Figure

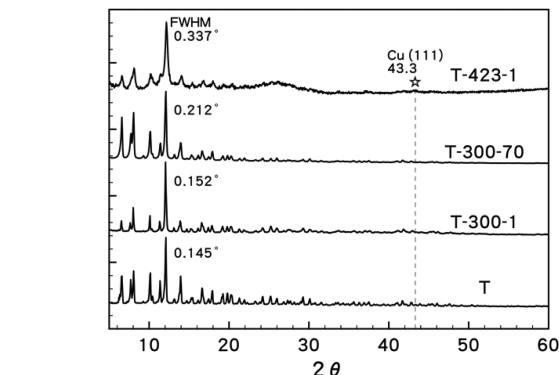


**Figure 3.** PXRD patterns of T after various H<sub>2</sub> exposures. The labeling is the same as that in Figure 2. A gradual broadening of the PXRD pattern is seen with H<sub>2</sub> exposure (see full-width half-maximum, Figure S3, Supporting Information). An indication of bulk Cu metal (star,  $2\theta = 43.2^\circ$ ) is found only after 423 K H<sub>2</sub> treatment.

2B) had two equal area (50:50) N peaks at 398.3 and 399.9 eV, assigned to the sp<sup>2</sup> N in the center ring aromatic heterocycles and the secondary-amine type NH in the branches, respectively. Assignments of FTIR modes associated with the Cu—O stretch and bend modes of the Cu PDW at 492 and 774 cm<sup>-1</sup> (Figure 4), respectively, were based on DFT calculations (Figure S5; see also S2, Supporting Information). The Cu—O assignments were consistent with other Cu—O bond frequencies found in the literature, typically between 500 and 600 cm<sup>-1</sup>.<sup>72–74</sup> The C—O asymmetric stretch for a carboxylate was found as a broad shoulder in the experimental data of the T series at 1642 cm<sup>-1</sup>. For comparison, the carboxylic acid H<sub>6</sub>TDPAT had a symmetric C—O stretch at 1250–1300 cm<sup>-1</sup> and a C=O stretch at 1680–1690 cm<sup>-1</sup>.<sup>57,58</sup> These acidic modes were significantly decreased in T.

Consistent with our previous report,<sup>50</sup> the PB doping technique did not significantly alter the characterization of the material prior to H<sub>2</sub> exposure: The XPS spectrum of PB-T

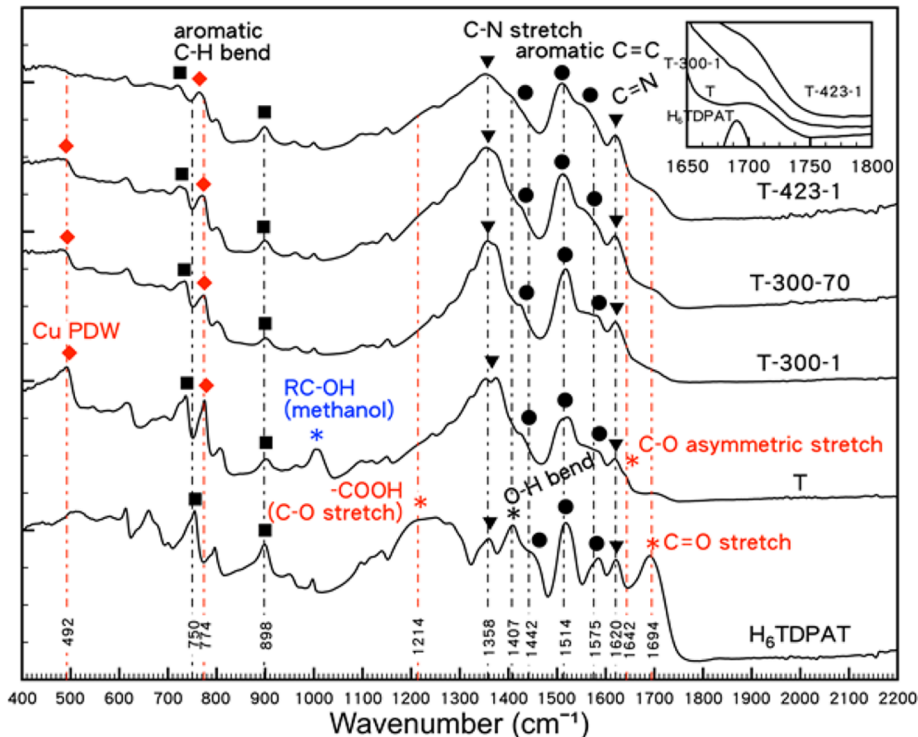


**Figure 4.** FTIR spectra of the organic ligand  $\text{H}_6\text{TDPAT}$  and  $\text{T}$  after various  $\text{H}_2$  exposures. Dotted lines indicate modes that vary (red) and do not vary (black) between samples. Additional labels are used to denote (◆) Cu related bond, (\*) O related bond, (▼) N related bond, (■) H related bond, and (●) C related bond.

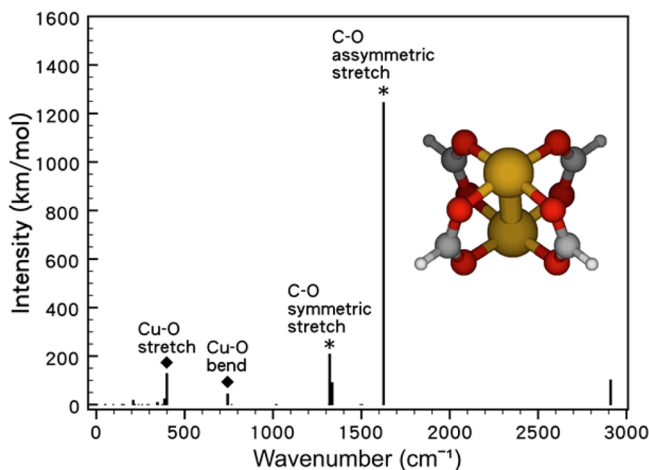


**Figure 5.** DFT calculated vibrational frequencies of the truncated Cu PDW terminated by formate (inset), with assignments as follows: (i)  $1625 \text{ cm}^{-1}$  is a C—O asymmetric stretch of the carboxylate, (ii)  $1320 \text{ cm}^{-1}$  is a C—O symmetric stretch of the carboxylate group, (iii)  $743 \text{ cm}^{-1}$  is a Cu—O bend, and (iv)  $399 \text{ cm}^{-1}$  is a Cu—O stretch. The mode at  $2900 \text{ cm}^{-1}$  is due to the C—H stretch of formate, and is thus not applicable to the  $\text{T}$  structure.

(Figure 6A, Figure S4, Supporting Information) was virtually identical to  $\text{T}$  (Figure 2, Figure S5, Supporting Information), as was the PXRD pattern (Figure 7). Notably, simple insertion of Pt/AC via the PB method leads to no discernible evidence for the creation of defects. The FTIR spectra (Figure 8) were also very similar, although there was a very minor blue shift in the asymmetric  $\text{C}=\text{O}$  mode of  $\text{PB-T}$  ( $\sim 1720 \text{ cm}^{-1}$ , see Figure 8 inset) relative to  $\text{T}$  ( $\sim 1700 \text{ cm}^{-1}$ , see Figure 4 inset). This blue-shift may be due to interaction with the inserted Pt/AC,

particularly as the asymmetric carboxylate  $\text{C}=\text{O}$  bonds are expected to be concentrated at defects and/or termination of the  $\text{T}$  crystal. A similar blue-shift was not seen for AC- $\text{T}$  (Figure S6, Supporting Information), suggesting the effect is due to Pt rather than carbon.

**3.1.2. High Temperature Dissociation of  $\text{T}$  into Its Components Is Catalyzed by Pt.** In order to later differentiate the effect of hydrogen spillover at 300 K, high temperature  $\text{H}_2$  reduction at 423 K was intended to represent the other extreme, namely, dissociation of  $\text{T}$  into Cu metal and the  $\text{H}_6\text{TDPAT}$  ligand. In our previous work,<sup>50</sup> thermogravimetric stability studies show  $\text{PB-T}$  slowly loses mass in 423 K  $\text{H}_2$ . Exposing undoped  $\text{T}$  to  $\text{H}_2$  at 423 K led to an irreversible reduction of Cu in XPS (Figure 2a), and in PXRD, a very slight indication of the formation of bulk Cu(111) metal at  $43.3^\circ$ <sup>75</sup> with broadening of the  $\text{T}$  pattern (Figure 3). Similar partial Cu reduction in XPS was observed previously for the closely related Cu-BTC, with an over 3-fold enhancement in the fraction of reduced Cu after merely heating to 420 K in a vacuum.<sup>76</sup> Cu reduction may be attributed to structural defects, in which a carboxylate ligand is displaced from the copper paddlewheel.<sup>71</sup> This explanation is consistent with the observed broadening of the PXRD pattern, if we presume defects are located at the termination of a crystallite, particularly as XPS is a surface-sensitive technique. FTIR of  $\text{T}$  after 423 K  $\text{H}_2$  showed loss of the Cu—O stretch mode at  $492 \text{ cm}^{-1}$ , the C—O asymmetric stretch at  $1642 \text{ cm}^{-1}$ , and an increase and red-shift (relative to  $\text{T}$ ) of the  $\text{C}=\text{O}$  stretch at  $1694 \text{ cm}^{-1}$  (Figure 4, inset). Other modes associated with the ligand remained intact in FTIR (black lines, Figure 4), as did the C and O 1s XPS modes (Figure S5, Supporting Information). Overall, the very subtle changes suggested a very small portion of  $\text{T}$  was dissociated by  $\text{H}_2$  reduction at 423 K. Elsewhere, high-temperature (423 K) reduction of the related Cu PDW present

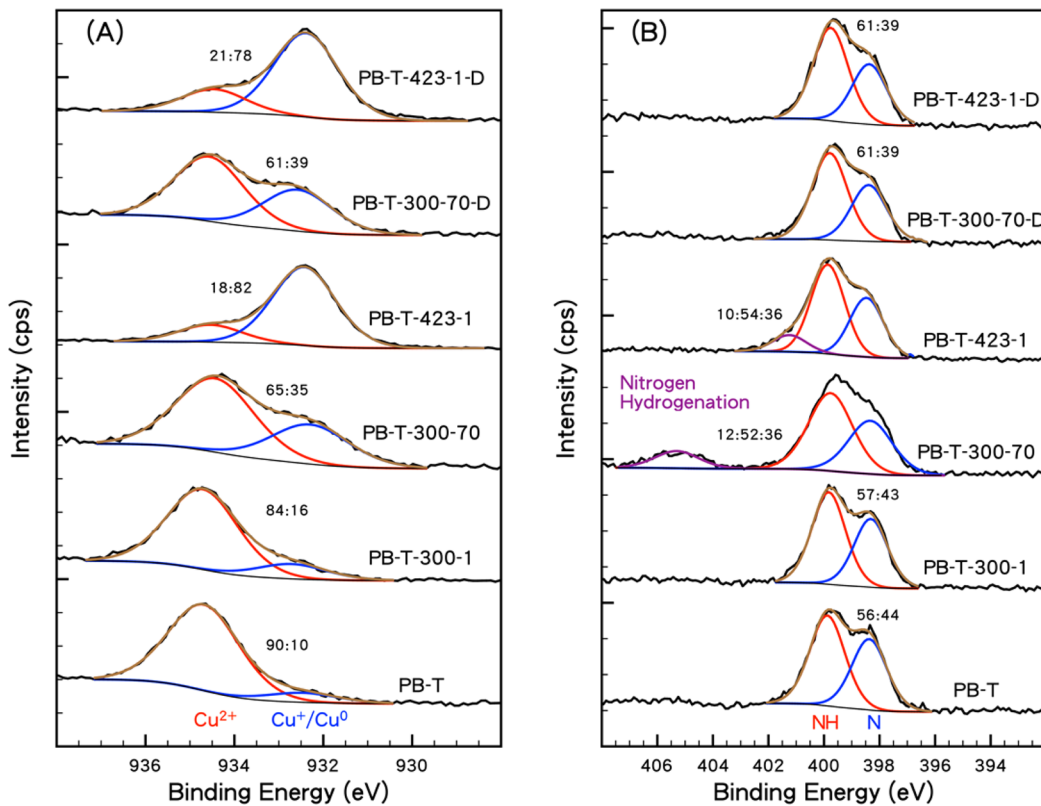


**Figure 6.** XPS spectra of prebridged Cu-TDPAT (PB-T) in (A) Cu 2p 3/2 and (B) N 1s. The subpeak ratio is listed. An increase in the  $\text{Cu}^+/\text{Cu}^0$  peak is observed after all exposures to  $\text{H}_2$ , while reversible nitrogen hydrogenation is observed for -300-70 and -423-1. The -D samples have been desorbed at 400 K in 1 bar argon.

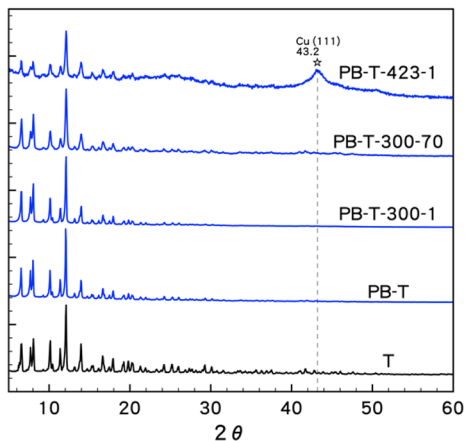


**Figure 7.** PXRD patterns of Cu-TDPAT (T), prebridged Cu-TDPAT with Pt/AC (PB-T), and the prebridged sample after hydrogen exposure of 300 K and 1 bar (PB-T-300-1), 300 K and 70 bar (PB-T-300-70), and 423 K and 1 bar (PB-T-423-1). Bulk Cu metal (star) is found only after 423 K  $\text{H}_2$  treatment.

in Cu-BTC was reported in the absence of catalyst,<sup>41,77</sup> but the stability is likely sensitive to both the ligand and the structural integrity.

Direct doping (DD) of Pt into the T structure via incipient wetness with a subsequent 423 K  $\text{H}_2$  reduction led to very pronounced broadening of the characteristic T pattern and a pronounced Cu(111) metal diffraction peak at  $43.4^\circ$ , as reported elsewhere.<sup>50</sup> Similarity between the  $\text{Cu}^{2+}:\text{Cu}^+/\text{Cu}^0$  ratios in XPS spectra of DD-T-423-1 (30:70, Figure 9A) and T-423-1 (25:75, Figure 2A), despite pronounced differences in the intensity of the

Cu(111) phase in PXRD, suggested the surface-sensitive XPS was not reflective of bulk Cu reduction. This corroborated the explanation given above; namely, the apparent irreversible Cu reduction detected in XPS was due to defects that occurred at the termination of T crystals.

The N 1s XPS spectrum of DD-T-423-1 showed a tertiary peak at 401.5 eV (Figure 9B, DD-T-423-1), which was not found in T-423-1. The feature was irreversible after heating DD-T-423-1 to 400 K in Ar (DD-T-423-1-D, Figure 9B), as was the Cu reduction observed in XPS. For N, a shift to higher binding energy was indicative of increasing hydrogen content.<sup>54</sup> As a similar mode was found in the  $\text{H}_6\text{TDPAT}$  precursor (Figure 9B), we suspected the 401.5 eV mode is indicative of a zwitterion effect; i.e., protonation of the secondary NH group by the carboxylic acid and similar shifts in the N 1s spectra have been observed for zwitterionic amino acids.<sup>78–80</sup> As will be discussed further below, DFT calculations suggested nitrogen hydrogenation was much more probable for a charged ligand, and thus, DFT was supportive of the zwitterionic assignment. Thus, we concluded direct introduction of Pt catalyzes dissociation of T into its components (i.e.,  $\text{H}_6\text{TDPAT}$  and bulk Cu metal) by  $\text{H}_2$  reduction at 423 K.

The “prebridge” (PB) Pt doping technique is a solvothermal method to introduce Pt/AC catalyst into the MOF synthesis solution prior to precipitation and crystal growth. Relative to DD-T-423-1, the Pt content of PB-T was reduced by 20-fold, and an intermediate AC surface was introduced between the Pt catalyst and the T surface. As shown previously, the PB method alleviated the need for high-temperature Pt reduction which can destabilize the MOF; thus, PB-T maintained the surface area and crystallinity of T, with only a minor reduction in the thermal

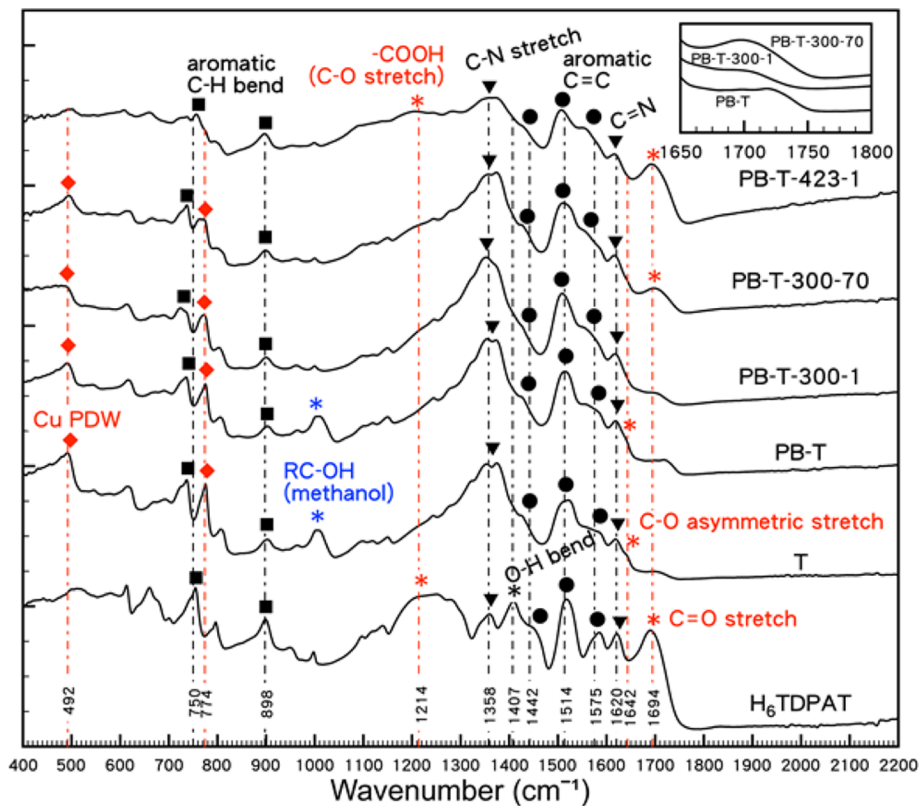


**Figure 8.** FTIR of the organic ligand  $\text{H}_6\text{TDPAT}$ , Cu-TDPAT (T), prebridged Cu-TDPAT with Pt/AC (PB-T), and the prebridged sample after hydrogen exposure of 300 K and 1 bar (PB-T-300-1), 300 K and 70 bar (PB-T-300-70), and 423 K and 1 bar (PB-T-423-1). Red legends indicate variations between samples. (◆) Cu related bond, (\*) O related bond, (▼) N related bond, (■) H related bond, (●) C related bond.

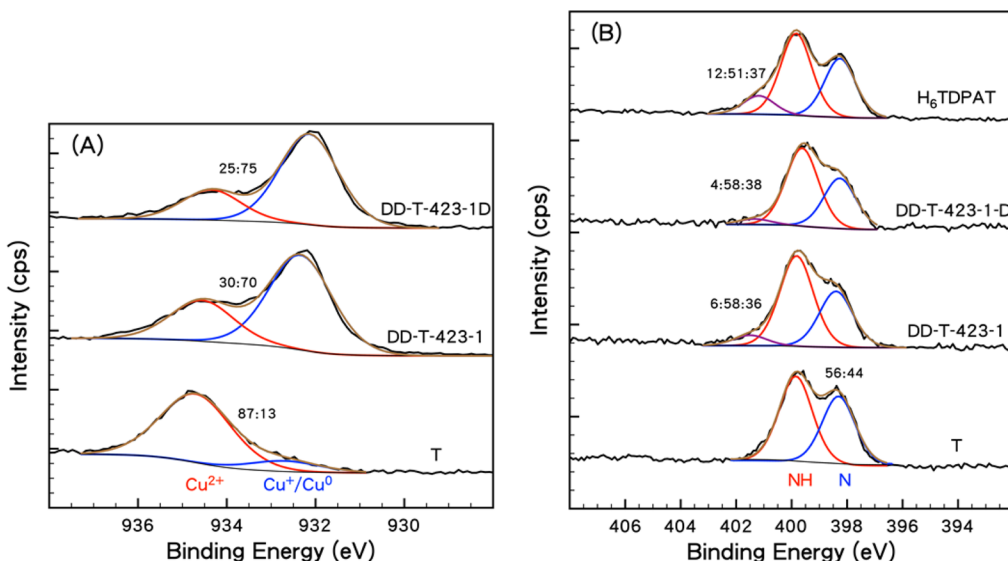


**Figure 9.** XPS spectra of direct-doped Pt on Cu-TDPAT (DD-T-423-1) in (A) Cu 2p 3/2 and (B) N 1s, with N 1s spectrum of organic ligand precursor  $\text{H}_6\text{TDPAT}$ . DD-T-423-1 has been reduced in 423 K  $\text{H}_2$  during synthesis. The subpeak ratio is listed. Copper reduction and nitrogen hydrogenation occurred after Pt reduction and were not reversible.

stability (i.e.,  $\sim 20$ – $25$  K shift in the thermogravimetric profiles, relative to the MOF precursor).<sup>50</sup> Here, catalyst insertion in PB-T has accelerated the structural dissociation and bulk Cu reduction at 423 K in  $\text{H}_2$  relative to T. However, the effect was significantly less pronounced than observed for DD-T-423-1. The Cu(111) diffraction of PB-T after 423 K  $\text{H}_2$  (Figure 7, PB-T-423-1) was less than that of DD-T-423-1<sup>50</sup> and greater than that

of T-423-1 (Figure 3). Further evidence for regeneration of carboxylic acid was found in the changing nature of the O 1s XPS (Figure S5, Supporting Information) and FTIR of PB-T-423-1. In FTIR, the COOH and asymmetric C=O stretch features (at  $1214$  and  $1694$   $\text{cm}^{-1}$ , respectively) become pronounced, and at high wavenumber, they closely resemble the  $\text{H}_6\text{TDPAT}$  ligand (Figure S1B, Supporting Information). The similarity between

the FTIR of PB-T-423-1 and H<sub>6</sub>TDPAT demonstrates the ligand was not degraded by 423 K H<sub>2</sub>, and in particular, the oxygen of the TDPAT ligand did not combine with H<sub>2</sub> to form water. Like DD-T-423-1, a zwitterionic 401.5 eV peak was found in N 1s XPS after 423 K H<sub>2</sub> (Figure 6B) and in high wavenumber FTIR (Figure S1B, Supporting Information). Unlike DD-T-423-1, however, this feature disappeared in the XPS spectra after heating to 400 K in Ar. The reversibility of this feature, combined with the intact T pattern in PXRD, suggested the PB-T structure was not fully degraded after 423 K H<sub>2</sub>. This can be attributed to a decreased transfer of H atoms to T due to the reduced Pt content and intermediate AC surface. Slower hydrogen transfer in PB-T can also account for the greater thermal stability of the PB technique relative to the DD technique.<sup>50</sup>

**3.1.3. Low Pressure H Chemisorption at 300 K, and the Effect of Pt.** Previously, we reported that the 300 K hydrogen adsorption of PB-T at 1 bar (5 cc/g STP) greatly exceeded (by a factor of 8) that expected for physisorption and chemisorption to the catalyst, and attributed this to hydrogen spillover (as reproduced in Figure 10).<sup>50</sup> Under comparable conditions, this

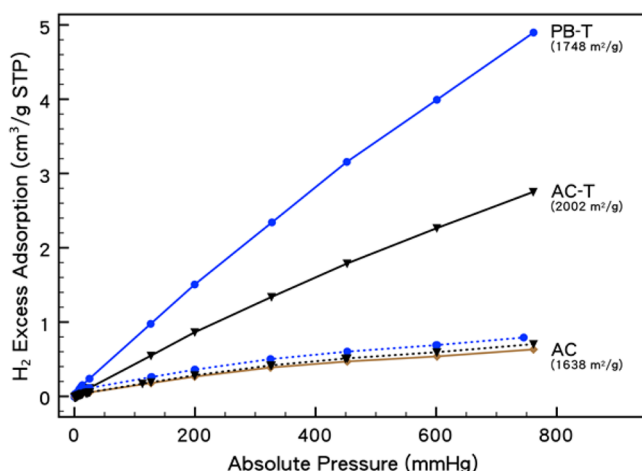


**Figure 10.** Hydrogen 300 K, 1 bar isotherms of activated carbon Maxsorb (AC), AC in Cu-TDPAT (T) via the prebridge method (AC-T), and prebridged Cu-TDPAT with Pt/AC (PB-T), with expected uptake (dotted lines) based on weighted average versus experimental data (solid line).

magnitude exceeded any previous reports of hydrogen uptake to MOFs after introduction of a catalyst (Supporting Information, Figure S7).<sup>12,19,81</sup> Under these conditions, the adsorption isotherms were reversible and cyclable (see Figure S8, Supporting Information); thus, the *ex situ* characterization techniques were unable to detect evidence for hydrogen chemisorption. The high level of hydrogen uptake for PB-T was at least partially attributable to defects introduced by incorporation of the Pt/AC particles, as AC-T (with no added Pt) also had uptake exceeding that expected (by a factor of 4) for physisorption to its components (Figure 10). The textural properties of AC-T were generally more favorable than PB-T for physisorption (i.e., the BET surface area was higher). A wider particle size distribution of the embedded AC relative to Pt/AC (see Figure S9, Supporting Information) increased the Cu defect ratio and the external surface area while decreasing the crystallite size (see Figures S4, S10, and S11 in the Supporting Information, respectively), and thus, AC-T was also more prone to hydrogenation of T at crystal termination sites. Thus, it seems

that both added Pt and introduced defects must be considered to account for the increased hydrogen uptake of PB-T relative to AC-T. Perhaps structural defects help to “seed” hydrogenation via a hole-mediated effect<sup>43</sup> while the heteroatoms contribute to partial ligand charging. Although it seems likely that incorporation of AC (and Pt/AC) contributed to structural instability and the creation of defects, the XPS, FTIR, XRD, and N<sub>2</sub> physisorption were relatively insensitive probes of defects (see the Supporting Information). Additional methods to characterize Cu-TDPAT defects, such as *in situ* FTIR probes of CO adsorption (as used previously for Cu-BTC<sup>71,82,83</sup>), are underway.

After the 300 K, 1 bar H<sub>2</sub> isotherm of T, surface reduction of Cu in XPS (Figure 2A) and broadening of the PXRD pattern (Figure 3) were observed, which were attributed to an increase in structural defects at the crystalline surface, for reasons discussed above. The effect was more pronounced for AC-T (see the Supporting Information, Figures S3 and S4), likely due to its smaller crystallite size. As before, the apparent surface Cu reduction was not reflective of bulk-phase reduction detected by PXRD, as no evidence for Cu<sup>0</sup> was found in PXRD (Figure 3). In FTIR, T-300-1 exhibited distortion of the Cu–O features and a subtle decrease in the C–O asymmetric stretch at 1642 cm<sup>-1</sup> (red lines, Figure 4); however, there was no indication that the carboxylate of T had converted to the acidic form. No other changes in the ligand were observed after exposing T to 1 bar H<sub>2</sub> at 300 K.

Insertion of Pt via the PB technique led to similar XPS, PXRD, and FTIR characterization results after 1 bar, 300 K H<sub>2</sub> exposure (i.e., comparing T-300-1 to PB-T-300-1). A more pronounced red-shift was observed in the C=O mode (1694 cm<sup>-1</sup>) of PB-T after 1 bar H<sub>2</sub> exposure (Figure 8, inset), relative to the T analogue (Figure 4, inset). However, like T-300-1, PB-T-300-1 did not show a significant increase in the acidic character of the carboxylate. Thus, 300 K H<sub>2</sub> has led to structural defects in PB-T, but the effect was comparable to undoped T. A parallel broadening of the PXRD pattern suggested the defects were located at the edge of crystallites.

**3.1.4. High Pressure H Chemisorption at 300 K, and the Effect of Pt.** Single-point adsorption measurements at 70 bar showed slow adsorption rates for five measurements of PB-T, including three batches with two sequential measurements (Figure 11). The adsorption amount for PB-T at long time ranged from 0.35 to 0.8 wt %. Some variation was seen between

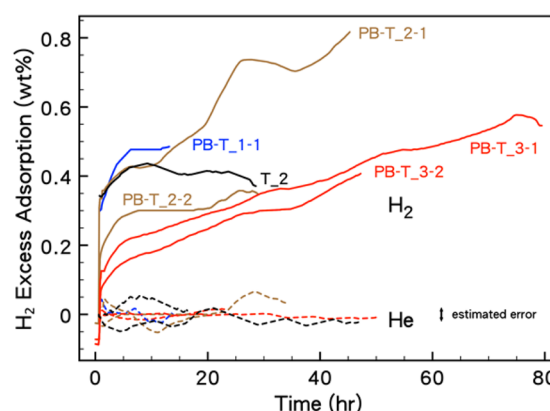


**Figure 11.** High-pressure H<sub>2</sub> and He kinetics of different batches of PB-T samples at 300 K. Numbers annotating sample names refer to the sample number followed by the sequential run number.

different PB-T batches, which can be attributed to slight variations in sample synthesis and catalytic doping. Subsequent runs on the same sample after intermittent pretreatment at 393 K showed some loss of capacity, 0.22 wt % for batch 2 and 0.035 wt % for batch 3; the latter was within the error bar of measurement. All of the H<sub>2</sub> adsorption rate curves were still increasing at the conclusion of the experiment (i.e., in excess of 60 h), showing more adsorption was likely with longer experimental time. Subsequent He measurements (dotted lines) showed this was observed only for PB-T in H<sub>2</sub>, and thus could not be attributed to leakage or cyclic temperature variations. Similarly, H<sub>2</sub> physisorption to T (black data, Figure 11) did not show the slow uptake with time. Although the final long-time uptake of PB-T exceeded that of T, the rate of uptake was prohibitively slow for PB-T. It is notable that the increased uptake of PB-T (relative to T) would not have been observed if short equilibration times had been used, and this issue would have been exacerbated for multiple step adsorption isotherms. (Multiple-step isotherms have a decrease in adsorption signal and also allow for equilibration of the sample in high-pressure hydrogen during sequential steps when the manifold is being charged.) Slow rates of adsorption can be attributed to activated diffusion with a particularly high activation barrier. For example, for H to travel 1 nm via activated diffusion, it would take 0.166 s if the barrier was 0.6 eV but 10 days if the barrier was 1 eV. (This estimate utilizes  $t = L^2/D$ ;  $D \sim 10^{-8} \exp[-E_A/RT] \text{ m}^2/\text{s}$ ; see also the Supporting Information.)

Further differentiation between T and PB-T, and spectroscopic evidence of H chemisorption in the presence of Pt, was found after the 70 bar, 300 K H<sub>2</sub> exposure of the high-pressure adsorption measurements. First, PB-T exhibited a new N 1s XPS mode that was at higher binding energy (405.3 eV) than previously observed (Figure 6B, PB-T-300-70). This mode was not found in T after comparable exposure (Figure 2B), demonstrating hydrogenation of this site was enabled by dissociation of H<sub>2</sub> by the Pt catalyst. However, the mode was not found for PB-T after 1 bar H<sub>2</sub> exposure, indicative of increasing access of hydrogenation sites at high pressure. The unique binding energy was suggestive of a new N–H binding site on the TDPAT ligand, particularly as no significant changes were observed in the C or O 1s XPS spectra that suggested N becomes bound to carbon or oxygen (Figure S5, Supporting Information). As the 401.5 eV was assigned to a zwitterion effect of the secondary-amine type NH in the branches, the mode of 405 eV was tentatively assigned to hydrogenation of the sp<sup>2</sup> N in the center ring. This feature was reversible after mild heating to 400 K in Ar (PB-T-300-70-D, Figure 6B), demonstrating hydrogen was weakly chemisorbed to this site. No sign of N–H hydrogenation was found in the high energy FTIR spectra (Figure S1B, Supporting Information), reflecting the low intensity of NH stretches relative to the predominant OH stretches, and perhaps suggesting this hydrogenation occurs only at the surface of the particle.

Second, FTIR of PB-T after 70 bar, 300 K H<sub>2</sub> exposure showed regeneration of the carboxylic acid character of the C–O modes (at 1694 cm<sup>-1</sup>), and additional evidence was found in the high wavenumber FTIR region (Figure S1B, Supporting Information) and the O 1s XPS spectra (Figure SSD, Supporting Information). Regeneration of the carboxylic acid character was not observed for T-300-70 (Figure 4). Unlike the dissociation found at 423 K (see section 3.1.2), the Cu–O modes in FTIR persisted (at 492 and 774 cm<sup>-1</sup>, Figure 8) and there was no sign of bulk Cu<sup>0</sup> in PXRD (Figure 7). The reappearance of features characteristic of

carboxylic acid without concomitant structural degradation of the Cu PDW implied hydrogenation between the carboxylate group and the Cu PDW, similar to what we described previously for the related Cu-BTC structure in the presence of a Pt/AC catalyst.<sup>8</sup> This is explored in more detail in section 3.2. Like the N case discussed in the previous paragraph, increasing evidence for hydrogenation at high pressure in the presence of Pt indicated increasing access of atomic H to the T surface at increasing pressure.

Furthermore, the 70 bar, 300 K H<sub>2</sub> exposure led to an increase in the reduced Cu of both T (the Cu<sup>2+</sup>:Cu<sup>+</sup>/Cu<sup>0</sup> ratio decreased from 87:13 to 59:41) and PB-T (90:10 to 65:35). The increase in fwhm of PXRD was also significant, nearly the same after the 423 K reduction (Figure 3 and Figure S3, Supporting Information). In several cases, the surface areas of both T and PB-T were significantly reduced after the high-pressure measurements, suggesting loss of the fraction of T that remained intact in the sample (see Table S1, Supporting Information). Loss of surface area after 1 bar H<sub>2</sub> adsorption measurements was not observed, nor was it observed after high-pressure (20 bar) He exposure. However, the pressure at which surface area was lost in high-pressure H<sub>2</sub> tended to be unpredictable (Table S1, Supporting Information). It appears that the loss of surface area seen after high-pressure H<sub>2</sub> exposure was due to mechanical instability, although this is somewhat speculative at this time.

Thus, there was spectroscopic evidence that the extent of PB-T hydrogenation was greater at 70 bar than at 1 bar: a new mode appeared in XPS that was attributed to hydrogenation of the central sp<sup>2</sup> N groups (Figure 6), and there was increasing carboxylic acid character including growth of the C=O stretch without destruction of the Cu–O stretch (Figure 8). The pressure dependence of hydrogen spillover has been highly debated in the field: Certain measurements exhibit adsorption isotherms that have not plateaued even at pressures in excess of 70 bar, whereas other laboratories have reported isotherms where the enhancement to hydrogen spillover was evident only at low pressure.<sup>27,28,32</sup> Part of the former could conceivably be associated with the incredibly slow rates of uptake observed here, as 40–60 h is well beyond the typical measurement time.<sup>10,84,85</sup> Furthermore, the spectroscopic evidence for additional hydrogenation sites at high pressures demonstrated atomic hydrogen had access to a greater surface at high pressure. However, the rate of hydrogenative adsorption to PB-T appeared prohibitively slow at high pressure, and structural instability accompanied high-pressure measurements.

**3.2. Density Functional Theory.** **3.2.1. Hydrogenation of the H<sub>6</sub>TDPAT Ligand.** Density functional theory calculations were used to establish trends for potential hydrogenation sites on the TDPAT ligand, using the H<sub>6</sub>TDPAT ligand (Figure 1) as an analogue for modeling. Although exclusion of the Cu PDW was an extreme simplification of the T structure, such structural truncations of MOFs are common in the literature, and it is also common to pin the external oxygen atoms in place in an attempt to mimic structural rigidity present in the crystal.<sup>42,43,86</sup> Up to 12 hydrogen molecules (24 H) could be exothermically added to the constrained H<sub>6</sub>TDPAT ligand ( $\Delta E = -0.55 \text{ eV/H}_2$ ), six per ring, and this introduced a minor strain energy ( $\sim 1 \text{ eV}$ ) in the ligand relative to the fully relaxed structure (Figure 12). Placement of H atoms on the secondary amine NH groups (i.e., N<sub>C</sub> in Figure 1) or the carbon of the carboxylate (C<sub>a</sub>) was endothermic.

Next, the overall order of hydrogenation on the organic ligand was calculated by determining the lowest energy hydrogenation

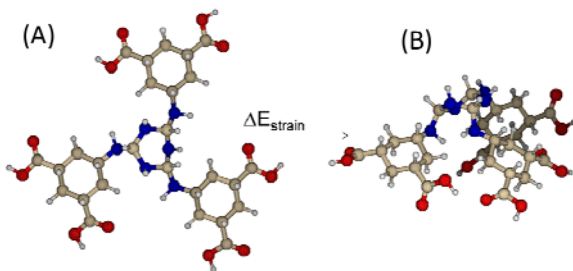


**Figure 12.** Density functional theory calculations to estimate total hydrogenation capacity, with external oxygens (A) held in place or (B) allowed to freely relax. The hydrogenation energies of these structures (adding 12 H<sub>2</sub> to the TDPAT ligand of Figure 1) are (A) −0.55 eV/H<sub>2</sub> and (B) −0.47 eV/H<sub>2</sub>, respectively, which corresponds to a strain energy of 0.96 eV.

site for each H addition (Table 1), considering the energy for each possible unique site. Placement of the first H atom (on C<sub>1</sub>)

**Table 1. Energy for Hydrogenation of the H<sub>6</sub>TDPAT Ligand at the SVP Level of Theory**

n <sub>H</sub> <sup>a</sup>	δE <sup>b</sup>	δ <sub>2</sub> E <sup>c</sup>	ΔE <sup>d</sup> (eV/H <sub>2</sub> )
1	−1.75		1.24
2	−2.84	0.15	0.15
3	−2.70	−0.80	−0.12
4	−3.11	−1.06	−0.46
5	−2.09	−0.46	−0.25
6	−3.91	−1.25	−0.72
7	−1.77	−0.93	−0.45
12	−3.89	ND <sup>e</sup>	−0.70
13	−1.86	−1.00	−0.57
18	−3.92	ND <sup>e</sup>	−0.70
19	−0.67	0.16	−0.49
20	−3.41	0.67	−0.57
21	−1.38	−0.04	−0.44
22	−3.24	0.12	−0.50
23	−1.44	0.06	−0.40
24	−3.45	−0.15	−0.47
25α	−0.52	0.77	−0.31
25β	−0.74	0.55	−0.32
25C	0.14	1.43	−0.25

<sup>a</sup>As labeled in Figure 1. <sup>b</sup>Incremental binding energy, with respect to atomic H:  $\delta E_n = E_n - E_{n-1} - E_H$ . <sup>c</sup>Incremental binding energy, with respect to molecular H<sub>2</sub>:  $\delta_2 E_n = E_n - E_{n-2} - E_{H_2}$ . <sup>d</sup>Overall hydrogenation energy, with respect to the pristine H<sub>6</sub>TDPAT ligand:  $\Delta E_n = (E_n - E_0 - (n/2)E_{H_2})/(n/2)$ . <sup>e</sup>ND: Not determined.

was endothermic with respect to H<sub>2</sub> ( $\Delta E = 1.24$  eV) but exothermic with respect to atomic H ( $\delta E = −1.75$  eV). Beyond the third H, hydrogenation of the structure relative to the initial reactants (i.e.,  $\Delta E$ ) was exothermic, even though addition of an H at a particular site was occasionally endothermic with respect to molecular hydrogen (i.e.,  $\delta E > −2.41$  eV, the calculated dissociation energy for H<sub>2</sub>). In particular, addition of an odd number of H atoms tended to be less favorable than addition of an even number of H atoms, which can be attributed to breaking the aromaticity and creation of an unpaired electron. The most favorable H addition was always the sixth H added to a ring. Similar trends for hydrogenation of other MOF structures have been reported previously.<sup>11,42,43,86,87</sup>

Hydrogenation of the outer carbon rings (“a”, Figure 1) was favored over hydrogenation of the inner C–N ring (“b”, Figure

1), and although addition of 24 H was exothermic (i.e.,  $\Delta E = −0.47$  eV/H<sub>2</sub>), the global energy minimum was after addition of 9 H<sub>2</sub> to the outer C rings ( $n = 18$ ,  $\Delta E = −0.70$  eV/H<sub>2</sub>). Furthermore, hydrogenation of H<sub>6</sub>TDPAT at the N<sub>C</sub> in the branch position was endothermic with respect to atomic H, regardless of whether it was the first H added ( $\delta E_1 = 0.23$  eV), the last H added ( $\delta E_{2S_2} = 0.14$  eV, Table 1), or the 19th H added ( $\delta E_{18C} = 0.007$  eV, Table 2). The latter scenario represents

**Table 2. Energy for Hydrogenation of the H<sub>6</sub>TDPAT Ligand at the SVP Level of Theory Based on Directional H Diffusion**

n <sub>H</sub> <sup>a</sup>	δE <sup>b</sup>	δ <sub>2</sub> E <sup>c</sup>	ΔE <sup>d</sup> (eV/H <sub>2</sub> )
6	−3.91	−1.25	−0.72
12 (two a rings)	−3.89	ND <sup>e</sup>	−0.70
18 (three a rings)	−3.92	ND <sup>e</sup>	−0.70
18+C	0.007	0.83	−0.42
18CCC	ND <sup>e</sup>	4.40	0.04
24C	0.14	1.43	−0.25

<sup>a</sup>As labeled in Figure 1. <sup>b</sup>Incremental binding energy, with respect to atomic H:  $\delta E_n = E_n - E_{n-1} - E_H$ . <sup>c</sup>Incremental binding energy, with respect to molecular H<sub>2</sub>:  $\delta_2 E_n = E_n - E_{n-2} - E_{H_2}$ . <sup>d</sup>Overall hydrogenation energy, with respect to the pristine H<sub>6</sub>TDPAT ligand:  $\Delta E_n = (E_n - E_0 - (n/2)E_{H_2})/(n/2)$ . <sup>e</sup>ND: Not determined.

surface diffusion “in” from the outer rings after full hydrogenation of the outer rings (gray arrows, Figure 1). The calculations suggest atomic H would prefer to be in the gas phase rather than chemically adsorbed to the N<sub>C</sub> branch site, suggesting that the N<sub>C</sub> branch site effectively serves as a “blockade” for surface diffusion. Thus, any experimental evidence for nitrogen hydrogenation was found only at high pressure or high temperature; furthermore, experimental evidence for nitrogen hydrogenation tends to be accompanied by partial T dissociation and/or creation of defects.

We also explored direct hydrogenation of a charged H<sub>6</sub>TDPAT ligand, with variations on the degree of prior hydrogenation. Partial charging of the ligand was intended to explore the effect of partial Cu reduction noted in the XPS above. For example, creation of a Cu<sup>2+</sup>/Cu<sup>+</sup> defect<sup>71</sup> from the Cu<sub>2</sub><sup>2+</sup> of the Cu PDW requires the addition of one electron, and would thus correspond to a positive charge on the TDPAT ligand (represented by L<sup>+</sup> in Table 3). Charging of the ligand would also be consistent with the zwitterionic effect suspected in the interpretation of the XPS data. Presuming the ligand was positively charged, a possible reaction sequence for subsequent hydrogenation, with corresponding reaction energies, is summarized in Table 3. Addition of the first H<sub>2</sub> to L<sup>+</sup> was

**Table 3. Calculation of Direct Hydrogenation Energies (from H<sub>2</sub>) for a Charged Ligand**

$LH_n^+ + H_2 \rightarrow LH_{n+2}^+$			
n <sup>a</sup>	lowest energy hydrogenation site <sup>a</sup>	$\delta_2 E_n^{+b}$ (eV)	$\delta_2 E_n$ (eV), uncharged <sup>c</sup>
0	H added to C <sub>1</sub> and C <sub>2</sub>	−0.27	0.15
17	H present on 1–17; added to C <sub>18</sub> and N <sub>C</sub>	−0.90	ND <sup>d</sup>
18	H present on 1–18; added to N <sub>C</sub> and C <sub>20</sub>	0.43	4.40

<sup>a</sup>As labeled in Figure 1. <sup>b</sup>For the reaction  $LH_n^+ + H_2 \rightarrow LH_{n+2}^+$ , with  $\delta_2 E_n^+ = E_{(n+2)+} - E_{(n)+} - E_{H_2}$ . <sup>c</sup>From Table 1:  $\delta_2 E_n = E_n - E_{n-2} - E_{H_2}$ . <sup>d</sup>ND: Not determined.

exothermic with respect to molecular H<sub>2</sub>, at  $-0.27$  eV, whereas the comparable energy in the uncharged case was endothermic at  $0.15$  eV. Addition of a H<sub>2</sub> to the N<sub>C</sub> position was not only possible for a charged ligand but was exothermic with respect to H<sub>2</sub>, at  $-0.90$  eV if the prior structure had 17 H atoms. If the prior structure had 18 H atoms, the addition of H<sub>2</sub> to LH<sub>18</sub><sup>+</sup> was mildly endothermic with respect to H<sub>2</sub> but significantly reduced relative to the uncharged case ( $0.43$  versus  $4.40$  eV, Table 3). Thus, charging of the ligand tended to make hydrogenation of the ligand more favorable in all studied cases, and even provided a feasible route to get H on the N<sub>C</sub> branch site via an exothermic reaction. Presuming the Cu<sup>2+</sup>/Cu<sup>+</sup> defects are concentrated at crystal termination sites, partial charging of the ligand may seed further hydrogenation. A related “hole-mediated” mechanism was put forth to explain the kinetics of hydrogen spillover in IRMOF-1.<sup>43</sup>

**3.2.2. Hydrogenation of the Cu–O–C Bond.** Insertion of two H atoms between two Cu–O bonds was exothermic for various “2H” isomers (see Figure 13), with a reaction energy of

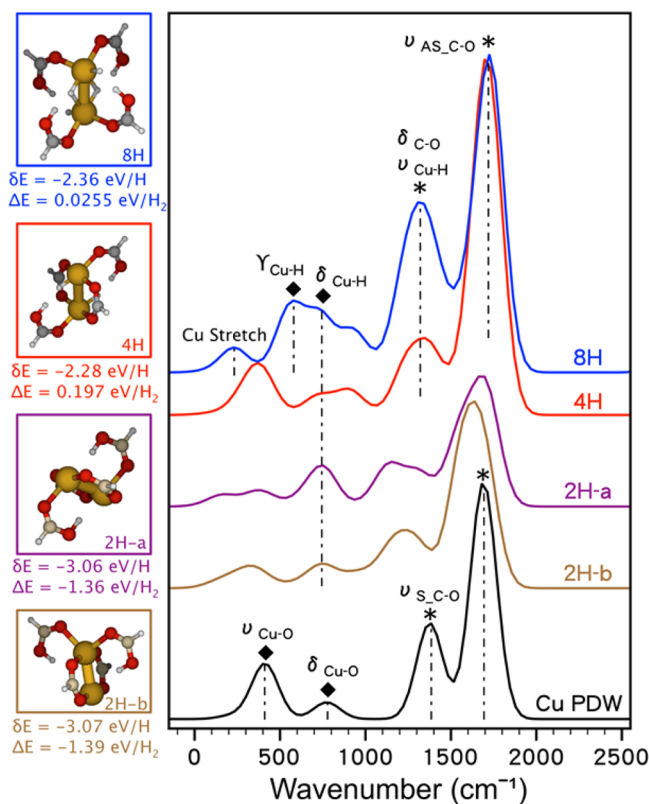


**Figure 13.** DFT calculated FTIR spectra of hydrogenated isomers of the Cu paddlewheel with formate ligands, as indicated. Calculated frequencies have been fitted to a Gaussian distribution. The truncated Cu paddlewheel is shown as an inset to Figure 1, and the 2H isomers (see inset) include (a) opposite-side, alternating H addition and (b) same-side, alternating H addition, respectively. Reaction energies are calculated with respect to atomic H ( $\delta E$ ) and molecular H<sub>2</sub> ( $\Delta E$ ). Other structures tested were either unstable or endothermic with respect to H<sub>2</sub>.

3.0–3.1 eV/H or  $\sim 1.4$  eV/H<sub>2</sub>. However, 2H isomers in which H was added on adjacent carboxylate groups (not shown) were unstable due to distortion caused by hydrogen bonding between the carboxylic acid and the neighboring oxygen group in the PDW. In contrast, isomers with alternating H addition led to less distortion of the truncated Cu PDW. In particular, alternating,

opposite-sided H addition (i.e., Figure 13a) led to a minor expansion in the plane of H addition (from  $5.07$  to  $6.85$  Å) and contraction in the other formate plane (to  $4.92$  Å) but did not significantly alter the length of the Cu–Cu bond. Although the distortions seen for the truncated cluster cannot be extrapolated to predict what might be seen in a periodic crystal, the minor expansion for the model structures helps to reconcile the FTIR data, demonstrating hydrogenation of the Cu–O–C bond in the T crystal, while PXRD data demonstrates the crystal remains intact.

No exothermic structures (with respect to H<sub>2</sub>) were found that included more than two H atoms. Notably then, the 2H isomers were consistent with the 1H:2COO ratio reported in our previous paper at a minimum pressure of 5 bar.<sup>8</sup> For the T ligand with the given Pt/AC content, the 0.3–0.8 wt % uptake (Figure 11) corresponds to a 1:0.9 to 1:2.5 H:COO ratio. The larger values, combined with the slow uptake, suggest hydrogenation occurs at both the ligand and the Cu–O–C bonding site, consistent with the XPS data that suggested hydrogenation of the central N group.

Calculated FTIR spectra of the 2H isomers (Figure 13) were consistent with conversion of a carboxylate to a carboxylic acid (i.e., the C–O symmetric stretch was significantly reduced and broadened in 2H, and there was a shift in the asymmetric stretch), and also showed distortion and significant broadening of the Cu–O modes (Figure 13). Both of these trends were observed experimentally. For comparison, calculated FTIR spectra of select endothermic “4H” and “8H” isomers, which included H both on the oxygen and on the Cu (see Figure 13), led to only minor shifts in the carbon–oxygen vibrational modes and the Cu–O stretch modes. A Cu–H mode was not observed when H was attached directly to Cu (i.e., 4H) but required some interaction with both Cu atoms to exhibit a notable Cu–H mode (8H, Figure 13). Furthermore, the exothermic proposed 2H isomers were generally consistent with the Cu reduction seen in XPS, as the number of bonds to the Cu atoms has decreased.

#### 4. SUMMARY AND CONCLUSIONS

The first goal of the paper was to use spectroscopic techniques to complement adsorption isotherms to provide site-specific evidence of hydrogen binding sites in PB-T. Evidence for hydrogen chemisorption was found at the following surface sites: (1) the sp<sup>2</sup> N aromatic heterocycles in the center ring, (2) the secondary-amine type NH in the branches, and (3) the Cu–O–C bond that connects the TDPAT ligand to the Cu PDW. A fourth potential binding site was the carbon atoms present in the TDPAT ligand, but the characterization techniques were relatively insensitive to C–H modes. Although the *ex situ* spectroscopic techniques probe only irreversible hydrogen binding sites, they provided evidence for hydrogenation of the TDPAT ligand at 300 K without full dissociation of T to Cu metal and H<sub>6</sub>TDPAT. Evidence for hydrogenation of (1) and (3) was found only in the presence of Pt in indirect contact with T (i.e., supported on AC), and thus confirmed the hydrogen spillover mechanism. Increasing hydrogenation of the TDPAT ligand was observed at higher pressure.

Hydrogen uptake of PB-T exceeded that expected for physisorption by a factor of 8, and was reversible and cyclable in low-pressure measurements. In addition to catalyst incorporation, the increased uptake was at least partially attributable to the introduction of defects. Hydrogen chemisorption to PB-T at 300 K was possible without structural degradation, although the structure degraded at higher temperatures and pressures.

Previous results<sup>50</sup> suggested this enhanced uptake required sufficient catalyst–MOF contact. Unfortunately, the Cu-TDPAT structure exhibited instabilities at high pressure, even without incorporated AC or Pt/AC. The instability and incredibly slow high pressure adsorption rates make this material an unsuitable candidate for practical hydrogen storage applications.

## ■ ASSOCIATED CONTENT

### Supporting Information

High wavenumber FTIR and rationale for assignments, fits of data, additional spectra and electron micrographs, calculations associated with adsorption isotherms and rates, and pressure stability tests for CuTDPAT. This material is available free of charge via the Internet at <http://pubs.acs.org>.

## ■ AUTHOR INFORMATION

### Corresponding Author

\*E-mail: adl11@psu.edu. Phone: (814) 863-6256. Fax: (814) 865-7846.

### Notes

The authors declare no competing financial interest.

## ■ ACKNOWLEDGMENTS

This work was supported by the U.S. Department of Energy, Energy Efficiency and Renewable Energy program, Award DE-FG36-08GO18139. The authors thank Julie Anderson in Materials Characterization Lab at the Pennsylvania State University for the assistance in SEM and FESEM. The computational work was supported through a Marie Curie International Incoming Fellowship (A.D.L.) and a Marie Curie International Reintegration Fellowship (G.P.).

## ■ REFERENCES

- (1) Eddaoudi, M.; Kim, J.; Rosi, N.; Vodak, D.; Wachter, J.; O'Keeffe, M.; Yaghi, O. M. Systematic Design of Pore Size and Functionality in Isoreticular MOFs and Their Application in Methane Storage. *Science* **2002**, *295*, 469–472.
- (2) Rosi, N. L.; Eckert, J.; Eddaoudi, M.; Vodak, D. T.; Kim, J.; O'Keeffe, M.; Yaghi, O. M. Hydrogen Storage in Microporous Metal-Organic Frameworks. *Science* **2003**, *300*, 1127–1129.
- (3) Rowsell, J. L. C.; Yaghi, O. M. Strategies for Hydrogen Storage in Metal-Organic Frameworks. *Angew. Chem., Int. Ed.* **2005**, *44*, 4670–4679.
- (4) <http://www1.eere.energy.gov/hydrogenandfuelcells/storage/>.
- (5) Lueking, A. D.; Yang, R. T. Hydrogen Spillover from a Metal Oxide Catalyst onto Carbon Nanotubes—Implications for Hydrogen Storage. *J. Catal.* **2002**, *206*, 165–168.
- (6) Lueking, A. D.; Yang, R. T. Hydrogen Storage in Carbon Nanotubes: Residual Metal Content and Pretreatment Temperature. *AIChE J.* **2003**, *49*, 1556–1568.
- (7) Conner, W. C.; Falconer, J. L. Spillover in Heterogeneous Catalysis. *Chem. Rev.* **1995**, *95*, 759–788.
- (8) Liu, X. M.; Rather, S.; Li, Q.; Lueking, A. D.; Zhao, Y.; Li, J. Hydrogenation of CuBTC Framework with the Introduction of a PtC Hydrogen Spillover Catalyst. *J. Phys. Chem. C* **2012**, *116*, 3477–3485.
- (9) Li, Y.; Yang, R. T. Significantly Enhanced Hydrogen Storage in Metal-Organic Frameworks via Spillover. *J. Am. Chem. Soc.* **2006**, *128*, 726–727.
- (10) Wang, C. Y.; Tsao, C. S.; Yu, M. S.; Liao, P. Y.; Chung, T. Y.; Wu, H. C.; Miller, M. A.; Tzeng, Y. R. Hydrogen Storage Measurement, Synthesis and Characterization of Metal-Organic Frameworks via Bridged Spillover. *J. Alloys Compd.* **2010**, *492*, 88–94.
- (11) Miller, M. A.; Wang, C. Y.; Merrill, G. N. Experimental and Theoretical Investigation Into Hydrogen Storage via Spillover in IRMOF-8. *J. Phys. Chem. C* **2009**, *113*, 3222–3231.
- (12) Li, Y.; Yang, R. T. Hydrogen Storage in Metal-Organic Frameworks by Bridged Hydrogen Spillover. *J. Am. Chem. Soc.* **2006**, *128*, 8136–8137.
- (13) Li, Y.; Yang, F. H.; Yang, R. T. Kinetics and Mechanistic Model for Hydrogen Spillover on Bridged Metal-Organic Frameworks. *J. Phys. Chem. C* **2007**, *111*, 3405–3411.
- (14) Tsao, C. S.; Yu, M. S.; Wang, C. Y.; Liao, P. Y.; Chen, H. L.; Jeng, U. S.; Tzeng, Y. R.; Chung, T. Y.; Wu, H. C. Nanostructure and Hydrogen Spillover of Bridged Metal-Organic Frameworks. *J. Am. Chem. Soc.* **2009**, *131*, 1404–1406.
- (15) Zlotea, C.; Campesi, R.; Cuevas, F.; Leroy, E.; Dibandjo, P.; Volkinger, C.; Loiseau, T.; Férey, G.; Latroche, M. Pd Nanoparticles Embedded into a Metal-Organic Framework: Synthesis, Structural Characteristics, and Hydrogen Sorption Properties. *J. Am. Chem. Soc.* **2010**, *132*, 2991–2997.
- (16) Park, S. J.; Lee, S. Y. A Study on Hydrogen-Storage Behaviors of Nickel-Loaded Mesoporous MCM-41. *J. Colloid Interface Sci.* **2010**, *346*, 194–198.
- (17) Stuckert, N. R.; Wang, L.; Yang, R. T. Characteristics of Hydrogen Storage by Spillover on Pt-Doped Carbon and Catalyst-Bridged Metal Organic Framework. *Langmuir* **2010**, *26*, 11963–11971.
- (18) Cao, W. X.; Li, Y. W.; Wang, L. M.; Liao, S. J. Effects of Metal Ions and Ligand Functionalization on Hydrogen Storage in Metal-Organic Frameworks by Spillover. *J. Phys. Chem. C* **2011**, *115*, 13829–13836.
- (19) Wang, L. F.; Stuckert, N. R.; Chen, H.; Yang, R. T. Effects of Pt Particle Size on Hydrogen Storage on Pt-Doped Metal-Organic Framework IRMOF-8. *J. Phys. Chem. C* **2011**, *115*, 4793–4799.
- (20) Lueking, A. D.; Yang, R. T. Hydrogen Spillover to Enhance Hydrogen Storage—Study of the Effect of Carbon Physicochemical Properties. *Appl. Catal., A* **2004**, *265*, 259–268.
- (21) Zieliński, M.; Wojcieszak, R.; Monteverdi, S.; Mercy, M.; Bettahar, M. M. Hydrogen Storage on Nickel Catalysts Supported on Amorphous Activated Carbon. *Catal. Commun.* **2005**, *6*, 777–783.
- (22) Lachawiec, A. J.; Qi, G.; Yang, R. T. Hydrogen Storage in Nanostructured carbons by Spillover: Bridge-Building Enhancement. *Langmuir* **2005**, *21*, 11418–11424.
- (23) Li, Y.; Yang, R. T. Hydrogen Storage on Platinum Nanoparticles Doped on Superactivated Carbon. *J. Phys. Chem. C* **2007**, *111*, 11086–11094.
- (24) Lachawiec, A. J.; Yang, R. T. Isotope Tracer Study of Hydrogen Spillover on Carbon-Based Adsorbents for Hydrogen Storage. *Langmuir* **2008**, *24*, 6159–6165.
- (25) Tsao, C. S.; Tzeng, Y. R.; Yu, M. S.; Wang, C. Y.; Tseng, H. H.; Chung, T. Y.; Wu, H. C.; Yamamoto, T.; Kaneko, K.; Chen, S. H. Effect of Catalyst Size on Hydrogen Storage Capacity of Pt-Impregnated Active Carbon via Spillover. *J. Phys. Chem. Lett.* **2010**, *1*, 1060–1063.
- (26) Tsao, C. S.; Liu, Y.; Chuang, H. Y.; Tseng, H. H.; Chen, T. Y.; Chen, C. H.; Yu, M. S.; Li, Q.; Lueking, A. D.; Chen, S. H. Hydrogen Spillover Effect of Pt-doped Activated Carbon Studied by Inelastic Neutron Scattering. *J. Phys. Chem. Lett.* **2011**, *2*, 2322–2325.
- (27) Psogogiannakis, G. M.; Steriotis, T. A.; Bourlinos, A. B.; Kouvelos, E. P.; Charalambopoulou, G. C. H.; Stubos, A. K.; Froudakis, G. E. Enhanced Hydrogen Storage by Spillover on Metal-Doped Carbon Foam: An Experimental and Computational Study. *Nanoscale* **2011**, *3*, 933–936.
- (28) Li, Q.; Lueking, A. D. Effect of Surface Oxygen Groups and Water on Hydrogen Spillover in Pt-Doped Activated Carbon. *J. Phys. Chem. C* **2011**, *115*, 4273–4282.
- (29) Li, Y.; Yang, R. T. Hydrogen Storage in Low Silica Type X Zeolites. *J. Phys. Chem. B* **2006**, *110*, 17175–17181.
- (30) Luzan, S. M.; Talyzin, A. V. Hydrogen Adsorption in Pt catalyst/MOF-5 Materials. *Microporous Mesoporous Mater.* **2010**, *135*, 201–205.
- (31) Campesi, R.; Cuevas, F.; Latroche, M.; Hirscher, M. Hydrogen Spillover Measurements of Unbridged and Bridged Metal-Organic Frameworks-Revisited. *Phys. Chem. Chem. Phys.* **2010**, *12*, 10457–10459.
- (32) Stadie, N. P.; Purewal, J. J.; Ahn, C. C.; Fultz, B. Measurements of Hydrogen Spillover in Platinum Doped Superactivated Carbon. *Langmuir* **2010**, *26*, 15481–15485.

- (33) Oh, H.; Gennett, T.; Atanassov, P.; Kurttepeli, M.; Bals, S.; Hurst, K. E.; Hirscher, M. Hydrogen Adsorption Properties of Platinum Decorated Hierarchically Structured Templatized Carbons. *Microporous Mesoporous Mater.* **2013**, *177*, 66–74.
- (34) Szilágyi, P. Á.; Callini, E.; Anastasopol, A.; Kwakernaak, C.; Sachdeva, S.; van de Krol, R.; Geerlings, H.; Borgschulte, A.; Züttel, A.; Dam, B. Probing Hydrogen Spillover in Pd@MIL-101(Cr) with a Focus on Hydrogen Chemisorption. *Phys. Chem. Chem. Phys.* **2014**, *16*, 5803–5809.
- (35) Nalwa, H. S. *Nanomaterials for energy storage applications*; American Scientific Publishers: Los Angeles, CA, 2009.
- (36) Mitchell, P. C. H.; Ramirez-Cuesta, A. J.; Parker, S. F.; Tomkinson, J.; Thompsett, D. Hydrogen Spillover on Carbon-Supported Metal Catalysts Studied by Inelastic Neutron Scattering. Surface Vibrational states and Hydrogen Riding Modes. *J. Phys. Chem. B* **2003**, *107*, 6838–6845.
- (37) Contescu, C. I.; Brown, C. M.; Liu, Y.; Bhat, V. V.; Gallego, N. C. Detection of Hydrogen Spillover in Palladium-Modified Activated Carbon Fibers During Hydrogen Adsorption. *J. Phys. Chem. C* **2009**, *113*, 5886–5890.
- (38) Blackburn, J. L.; Engtrakul, C.; Bult, J. B.; Hurst, K.; Zhao, Y.; Xu, Q.; Parilla, P. A.; Simpson, L. J.; Rocha, J.-D. R.; Hudson, M. R.; et al. Spectroscopic Identification of Hydrogen Spillover Species in Ruthenium-Modified High Surface Area Carbons by Diffuse Reflectance Infrared Fourier Transform Spectroscopy. *J. Phys. Chem. C* **2012**, *116*, 26744–26755.
- (39) Liu, X. M.; Tang, Y.; Xu, E. S.; Fitzgibbons, T. C.; Larsen, G. S.; Gutierrez, H. R.; Tseng, H. H.; Yu, M. S.; Tsao, C. S.; Badding, J. V.; et al. Evidence for Ambient-Temperature Reversible Catalytic Hydrogenation in Pt-doped Carbons. *Nano Lett.* **2013**, *13*, 137–141.
- (40) Lueking, A. D.; Psوفogiannakis, G.; Froudakis, G. E. Atomic Hydrogen Diffusion on Doped and Chemically Modified Graphene. *J. Phys. Chem. C* **2013**, *117*, 6312–6319.
- (41) Chen, H.; Wang, L.; Yang, J.; Yang, R. T. Investigation on Hydrogenation of Metal Organic Frameworks HKUST-1, MIL-53 and ZIF-8 by Hydrogen Spillover. *J. Phys. Chem. C* **2013**, *117*, 7565–7576.
- (42) Suri, M.; Dornfeld, M.; Ganz, E. Calculation of Hydrogen Storage Capacity of Metal-Organic and Covalent-Organic Frameworks by Spillover. *J. Chem. Phys.* **2009**, *131*, 174703.
- (43) Lee, K.; Kim, Y. H.; Sun, Y. Y.; West, D.; Zhao, Y.; Chen, Z.; Zhang, S. B. Hole-Mediated Hydrogen Spillover Mechanism in Metal-Organic Frameworks. *Phys. Rev. Lett.* **2010**, *104*, 236101.
- (44) Psوفogiannakis, G. M.; Froudakis, G. E. Theoretical Explanation of Hydrogen Spillover in Metal-Organic Frameworks. *J. Phys. Chem. C* **2011**, *115*, 4047–4053.
- (45) Mulfort, K. L.; Hupp, J. T. Alkali Metal Cation Effects on Hydrogen Uptake and Binding in Metal-Organic Frameworks. *Inorg. Chem.* **2008**, *47*, 7936–7938.
- (46) Xiang, Z.; Hu, Z.; Yang, W.; Cao, D. Lithium Doping on Metal-Organic Frameworks for Enhancing H<sub>2</sub> Storage. *Int. J. Hydrogen Energy* **2011**, *37*, 946–950.
- (47) Gao, S.; Zhao, N.; Shu, M.; Che, S. Palladium Nanoparticles Supported on MOF-5: A Highly Active Catalyst for a Ligand-and Copper-free Sonogashira Coupling Reaction. *Appl. Catal., A* **2010**, *388*, 196–201.
- (48) Sabo, M.; Henschel, A.; Fröde, H.; Klemm, E.; Kaskel, S. Solution Infiltration of Palladium into MOF-5: Synthesis, Physisorption and Catalytic Properties. *J. Mater. Chem.* **2007**, *17*, 3827–3832.
- (49) Esken, D.; Zhang, X.; Lebedev, O. I.; Schröder, F.; Fischer, R. A. Pd@ MOF-5: Limitations of Gas-Phase Infiltration and Solution Impregnation of [Zn<sub>4</sub>O (bdc)<sub>3</sub>](MOF-5) with Metal-Organic Palladium Precursors for Loading with Pd Nanoparticles. *J. Mater. Chem.* **2009**, *19*, 1314–1319.
- (50) Wang, C. Y.; Gong, Q.; Zhao, Y.; Li, J.; Lueking, A. D. Stability and Catalytic Activity of Metal-Organic Frameworks Prepared via Different Catalyst Doping Methods. *J. Catal.* **2014**, *318*, 128–142.
- (51) Yang, S. J.; Cho, J. H.; Nahm, K. S.; Park, C. R. Enhanced Hydrogen Storage Capacity of Pt-loaded CNT@ MOF-5 Hybrid Composites. *Int. J. Hydrogen Energy* **2010**, *35*, 13062–13067.
- (52) Lee, S. Y.; Park, S. J. Effect of Platinum Doping of Activated Carbon on Hydrogen Storage Behaviors of Metal-Organic Frameworks-5. *Int. J. Hydrogen Energy* **2011**, *36*, 8381–8387.
- (53) Li, B.; Zhang, Z.; Li, Y.; Yao, K.; Zhu, Y.; Deng, Z.; Yang, F.; Zhou, X.; Li, G.; Wu, H.; et al. Enhanced Binding Affinity, Remarkable Selectivity, and High Capacity of CO<sub>2</sub> by Dual Functionalization of a rht-type Metal-Organic Framework. *Angew. Chem., Int. Ed.* **2012**, *51*, 1412–1415.
- (54) Moulder, J. F.; Chastain, J. *Handbook of X-Ray Photoelectron Spectroscopy: A Reference Book of Standard Spectra for Identification and Interpretation of XPS Data*; Perkin-Elmer Corporation, Physical Electronics Division: Eden Prairie, Minnesota, 1992.
- (55) Yu, D. L.; He, J. L.; Liu, Z. Y.; Xu, B.; Li, D. C.; Tian, Y. J. Phase Transformation of Melamine at High Pressure and Temperature. *J. Mater. Sci.* **2008**, *43*, 689–695.
- (56) <http://vpl.astro.washington.edu/spectra/methanolpnlimages.htm>.
- (57) Vollhardt, K. P. C.; Schore, N. E. *Organic Chemistry: Structure and Function*; W. H. Freeman: New York, 1998.
- (58) [http://en.wikipedia.org/w/index.php?title=Infrared\\_spectroscopy\\_correlation\\_table=541738594](http://en.wikipedia.org/w/index.php?title=Infrared_spectroscopy_correlation_table=541738594).
- (59) Costa, L.; Camino, G. Thermal Behaviour of Melamine. *J. Therm. Anal. Calorim.* **1988**, *34*, 423–429.
- (60) McMurry, J. *Organic Chemistry*; International edition; Brooks/Cole Cengage Learning: Belmont, CA, 2012.
- (61) Wang, J.; Rangel, E. C.; da Cruz, N. C.; Swart, J. W.; de Moraes, M. A. Amorphous Carbon Nitride Films Irradiated with Argon Ions. *Nucl. Instrum. Methods Phys. Res., Sect. B* **2000**, *166*, 420–425.
- (62) Sircar, S.; Wang, C.-Y.; Lueking, A. D. Design of High Pressure Differential Volumetric Adsorption Measurements with Increased Accuracy. *Adsorption* **2013**, 1–24.
- (63) Eichkorn, K.; Treutler, O.; Öhm, H.; Häser, M.; Ahlrichs, R. Auxiliary Basis Sets to Approximate Coulomb Potentials. *Chem. Phys. Lett.* **1995**, *240*, 283–290.
- (64) Becke, A. D. Density-functional Exchange-Energy Approximation with Correct Asymptotic Behavior. *Phys. Rev. A* **1988**, *38*, 3098–3100.
- (65) Perdew, J. P. Density-Functional Approximation for the Correlation Energy of the Inhomogeneous Electron Gas. *Phys. Rev. B* **1986**, *33*, 8822–8824.
- (66) Weigend, F.; Ahlrichs, R. Balanced Basis Sets of Split Valence, Triple Zeta Valence and Quadruple Zeta Valence Quality for H to Rn: Design and Assessment of Accuracy. *Phys. Chem. Chem. Phys.* **2005**, *7*, 3297–3305.
- (67) Neese, F. Prediction of Molecular Properties and Molecular Spectroscopy with Density Functional Theory: From Fundamental Theory to Exchange-Coupling. *Coord. Chem. Rev.* **2009**, *253*, 526–563.
- (68) Weymuth, T.; Couzijn, E. P. A.; Chen, P.; Reiher, M. New Benchmark Set of Transition-Metal Coordination Reactions for the Assessment of Density Functionals. *J. Chem. Theory Comput.* **2014**, *10*, 3092–3103.
- (69) Laury, M. L.; Carlson, M. J.; Wilson, A. K. Vibrational Frequency Scale Factors for Density Functional Theory and the Polarization Consistent Basis Sets. *J. Comput. Chem.* **2012**, *33*, 2380–2387.
- (70) Ahlrichs, R.; Bär, M.; Häser, M.; Horn, H.; Kölmel, C. Electronic Structure Calculations on Workstation Computers: The program System Turbomole. *Chem. Phys. Lett.* **1989**, *162*, 165–169.
- (71) St Petkov, P.; Vayssilov, G. N.; Liu, J.; Shekhah, O.; Wang, Y.; Wöll, C.; Heine, T. Defects in MOFs: A Thorough Characterization. *ChemPhysChem* **2012**, *13*, 2025–2029.
- (72) Yeşilel; Paşaoglu; Akdag; Büyükgüngör. The First bis(orotate-N,O) Complex: Synthesis, Crystal Structure, Spectroscopic and Thermal Characterization of (chaH)<sub>2</sub>[Cu(HOr-N,O)<sub>2</sub>(cha)]·2H<sub>2</sub>O (cha=cyclohexylamine and HOr=orotate(2-)). *Polyhedron* **2007**, *26*, 2761–2766.
- (73) Gasque, L.; Medina, G.; Ruiz-Ramírez, L.; Moreno-Esparza, R. Cu-O Stretching Frequency Correlation with Phenanthroline pKa Values in Mixed Copper Complexes. *Inorg. Chim. Acta* **1999**, *288*, 106–111.

- (74) Jin, W. T.; Hao, S. J.; Wang, C. X.; Guo, C. Q.; Xia, L.; Zhang, S. L.; Narlikar, A. V.; Zhang, H. Structural and Spectroscopic Evidence for Stable Chemical Bonds and the Correlation with High Tc Superconductivity. *Supercond. Sci. Technol.* **2012**, *25*, 065004.
- (75) Habibi, M. H.; Kamrani, R.; Mokhtari, R. Fabrication and Characterization of Copper Nanoparticles Using Thermal Reduction: The Effect of Nonionic Surfactants on Size and Yield of Nanoparticles. *Microchim. Acta* **2010**, *171*, 91–95.
- (76) Shekhah, O.; Liu, J.; Fischer, R. A.; Wöll, C. H. MOF Thin Films: Existing and Future Applications. *Chem. Soc. Rev.* **2011**, *40*, 1081–1106.
- (77) Grzech, A.; Yang, J.; Dingemans, T. J.; Srinivasan, S.; Magusin, P.; Mulder, F. M. Irreversible High-Temperature Hydrogen Interaction with the Metal Organic Framework Cu<sub>3</sub>(BTC)<sub>2</sub>. *J. Phys. Chem. C* **2011**, *115*, 21521–21525.
- (78) For example, from 399.5 to 401.5 eV in L-cysteine/Au(110) and to 401.5 eV in L-methionine nanogratings on the Ag(111). Schiffrin, A.; Riemann, A.; Auwärter, W.; Pennec, Y.; Weber-Bargioni, A.; Cvetko, D.; Cossaro, A.; Morgante, A.; Barth, J. V. Zwitterionic Self-Assembly of L-methionine Nanogratings on the Ag(111) Surface. *Proc. Natl. Acad. Sci. U. S. A.* **2007**, *104*, 5279–5284.
- (79) From 401.2–401.3 eV for NH<sub>3</sub><sup>+</sup> on L-methionine amino acid on Ag(111) and on Cu(111) to 402.2 eV for protonated NH<sub>3</sub> on L-tyrosine on Ag(111). Reichert, J.; Schiffrin, A.; Auwärter, W.; Weber-Bargioni, A.; Marschall, M.; Dell'angela, M.; Cvetko, D.; Baydek, G.; Cossaro, A.; Morgante, A.; Barth, J. V. L-tyrosine on Ag(111): Universality of the Amino Acid 2D Zwitterionic Bonding scheme? *ACS Nano* **2010**, *4*, 1218–1226.
- (80) From 399.1 eV (NH<sub>2</sub>) to 401.4 (NH<sub>2</sub>-H<sup>δ+</sup>) to 402.2 eV (NH<sub>3</sub><sup>+</sup>) for glycine on Si(111). Zhang, L.; Chatterjee, A.; Ebrahimi, M.; Leung, K. T. Hydrogen-Bond Mediated Transitional Adlayer of Glycine on Si(111)7 × 7 at Room Temperature. *J. Chem. Phys.* **2009**, *130*, 121103.
- (81) Li, Y.; Yang, R. T. Hydrogen Storage in Metal-Organic and Covalent-Organic Frameworks by Spillover. *AICHE J.* **2008**, *54*, 269–279.
- (82) Drenchev, N.; Ivanova, E.; Mihaylov, M.; Hadjiivanov, K. CO as an IR Probe Molecule for Characterization of Copper Ions in a Basolite C300 MOF Sample. *Phys. Chem. Chem. Phys.* **2010**, *12*, 6423–6427.
- (83) Szanyi, J.; Daturi, M.; Clet, G.; Baer, D. R.; Peden, C. H. Well-studied Cu-BTC Still Serves Surprises: Evidence for Facile Cu<sup>2+</sup>/Cu<sup>+</sup> Interchange. *Phys. Chem. Chem. Phys.* **2012**, *14*, 4383–4390.
- (84) Bhat, V. V.; Contescu, C. I.; Gallego, N. C.; Baker, F. S. Atypical Hydrogen Uptake on Chemically-Activated, Ultramicroporous Carbon. *Carbon* **2010**, *48*, 1331–1340.
- (85) Bhat, V. V.; Contescu, C. I.; Gallego, N. C. Kinetic Effect of Pd Additions on the Hydrogen Uptake of Chemically-Activated Ultramicroporous Carbon. *Carbon* **2010**, *48*, 2361–2380.
- (86) Psوفogiannakis, G. M.; Froudakis, G. E. DFT Study of the Hydrogen Spillover Mechanism on Pt-Doped Graphite. *J. Phys. Chem. C* **2009**, *113*, 14908–14915.
- (87) Mavrandonakis, A.; Klopper, W. Comment on “Kinetics and Mechanistic Model for Hydrogen Spillover on Bridged Metal-Organic Frameworks. *J. Phys. Chem. C* **2008**, *112*, 3152–3154.